NASA Technical Paper 2914

1989

A Review of High-Speed, Convective, Heat-Transfer Computation Methods

Michael E. Tauber
Ames Research Center
Moffett Field, California

National Aeronautics and Space Administration
Office of Management
Scientific and Technical Information Division

NOMENCLATURE

B	mass-addition parameter (Eq. 70)
C	mass concentration
C_1	constant in Eq. 37
c_f	skin-friction coefficient
c_p	specific heat at constant pressure
D	binary diffusion coefficient
F	diffusion function (Eq. 6)
f	similarity stream function (Eq. 13)
g	total enthalpy ratio, H/H_e
H	total enthalpy, $h + (u^2 + w^2)/2$
H	cavity depth (Eq. 65)
h	static enthalpy
h'	reference enthalpy (Eq. 53)
j	exponent (j = 0 for yawed, infinite cylinder; j = 1 for axisymmetric body)
k	coefficient of thermal conductivity
k	roughness element height (Eq. 50)
L	cavity length (Eq. 65)
Le	Lewis number, $\rho c_p D/k_f$
M	Mach number
$\dot{m}$	mass addition rate
$\bar{m}$	molecular weight of gas
Nu	Nusselt number, $\dot{q}_w c_p x/k(h_{aw} - h_w)$
Pr	Prandtl number, $\mu c_p/k$
p	pressure
p_p	peak pressure (Eq. 68)
p_s	stagnation pressure
q_w	heat transfer rate to the body surface
r	radius of body of revolution
r_n	nose radius of hemisphere
$\bar{r}$	enthalpy recovery factor
R	gas constant
Re	Reynolds number, $\rho u x/\mu$
St	Stanton number, $\dot{q}_w/\rho_e u_e(h_{aw} - h_w)$
t	static enthalpy normalized by total enthalpy at boundary layer edge, h/H_e
u,v,w	velocity components in the x,y,z directions, respectively
V_∞	free-stream velocity
x,y,z	chordwise, normal, and spanwise coordinates
Z	Compressibility factor
α	angle of attack
β	pressure gradient parameter (Eq. 21)
Γ	heat-transfer function ratio (Eq. 43)
γ	specific heat ratio
δ	cone half angle, wedge angle, or flat-plate angle with respect to free stream
ε	inverse density ratio across shock, ρ_∞/ρ_e
θ	boundary layer momentum thickness
Λ	sweep, or yaw, angle of wing leading edge or cylinder
μ	coefficient of viscosity
μ_0	reference value of coefficient of viscosity
ξ,η	similarity variables (Eq. (9-10))
ρ	density of gas
φ	density and viscosity product ratio (Eq. 17)
ψ	stream function (Eq. 11)
Ψ	ratio of heat transfer at surface with mass addition to value without mass addition (coldwall value) (Eq. 69)
ζ	spanwise velocity ratio, w/w_e

Subscripts

A,M	atoms and molecules in binary mixture
aw	adiabatic wall (no heat transfer at wall)
bt	beginning of boundary layer transition
c	cone
cyl	cylinder
e	value at boundary layer edge
f	chemically frozen value
FP	flat plate
s	stagnation point value
SL	stagnation line
w	wall, or local body surface, value
∞	free-stream conditions

SUMMARY

The objective of this report is to provide useful engineering formulations and to instill a modest degree of physical understanding of the phenomena governing convective aerodynamic heating at high flight speeds. Some physical insight is not only essential to the application of the information presented here, but also to the effective use of computer codes which may be available to the reader. The paper begins with a discussion of cold-wall, laminar boundary layer heating. A brief presentation of the complex boundary layer transition phenomenon follows. Next, cold-wall turbulent boundary layer heating is discussed. This topic is followed by a brief coverage of separated flow-region and shock-interaction heating. A review of heat protection methods follows, including the influence of mass addition on laminar and turbulent boundary layers. The paper concludes with a discussion of finite-difference computer codes and a comparison of some results from these codes. An extensive list of references is also provided from sources such as the various AIAA journals and NASA reports which are available in the open literature.

1. INTRODUCTION

The original impetus for developing means of predicting the aerodynamic heating during high-speed atmospheric flight was the advent of the long-range missile. Only a modest extension of technology was required from the missile atmospheric entry velocity of about 6 km/sec to the 7.5-km/sec entry speed of vehicles returning from satellite orbit. It is the fortuitous behavior of air molecules at high temperatures that made the early formulations of aerodynamic heating applicable to a speed of about 9 km/sec, thereby covering both the missile and satellite entry flight regime.

The pioneering papers of Lees (ref. 1) and Fay and Riddell (ref. 2), published in 1956 and 1958, respectively, provided the basic physical and mathematical modeling for hypervelocity convective aerodynamic heating. However, the early work (refs. 1 and 2) was hampered by a lack of information of the high-temperature thermodynamic and transport properties of air. Succeeding computations by Beckwith and Cohen (ref. 3) and Cohen (ref. 4), published in 1961, used the high-temperature thermodynamic properties of Moeckel and Weston (ref. 5) and the transport properties of Hansen (ref. 6), both published in 1958. The state of the art in convective heat transfer at hypersonic speeds in the early 1960s was well presented by Dorrance (ref. 7). Possibly the best current source of information for the working engineer is the chapter on forced convection in external flows by Rubesin et al. (ref. 8).

In a high-velocity flow, the physical mechanism of heat transfer differs from the molecular heat-conduction process occurring at lower speeds. At sufficiently high speeds, the air that has passed through the strong shock wave surrounding the front of the body becomes so hot that the molecules dissociate into atoms. When the atoms diffuse through the boundary layer into the cooler region near the wall, the heat of recombination that is released as molecules form can contribute significantly to the heating of the wall. Therefore, at high speeds convective heating consists of both conduction and diffusion (due to atomic recombination) of energy through the boundary layer. The ratio of energy transported by diffusion to that by conduction is known as the Lewis number and is an important parameter in high-speed, laminar, boundary layer calculations. The chemical reactions in the laminar boundary layer are frequently frozen at altitudes in excess of about 45 km according to Fay (ref. 9). Therefore, the heating can be potentially reduced (ref. 2) if the wall is made of a noncatalytic, glassy, or ceramic material which inhibits atom recombination. For example, Rakich et al. (ref. 10) have shown that the Shuttle orbiter tiles are noncatalytic. Metals and many ablative heat-shield materials that are widely used on missiles are catalytic; therefore, finite-rate catalytic effects will not be considered in the following discussions. Wall catalysis effects are included in the finite-difference boundary layer and surface material interactions computer codes which will be mentioned later.

The objective of this review is to provide useful engineering formulations and to instill a modest degree of physical understanding of the phenomena governing convective aerodynamic heating. Some physical insight is not only essential to the application of the information presented here, but also to the effective use of computer codes which may be available to the reader. (In many codes, the physics are obscured by the mathematical procedure required to solve the differential equations.) An extensive list of references is also provided from sources such as the various AIAA journals and NASA reports which are available in the open literature.

The paper begins with a discussion of cold-wall, laminar boundary layer heating. (The term "cold wall" means that no mass addition occurs at the body surface and that the influence of the wall affects the heating only

through the temperature of the wall.) A brief presentation of the complex boundary layer transition phenomenon follows. Next, cold-wall turbulent boundary layer heating is discussed. This topic is followed by a brief coverage of separated flow-region heating. A review of heat protection methods follows, including the influence of mass addition on laminar and turbulent boundary layers. The report concludes with a discussion of comparisons and some results from finite-difference computer codes.

Within the text of the report, the MKS metric system of units is used. However, most of the figures that are shown originated in other papers and are not replotted if English units were originally used. Therefore, conversion factors are presented in the Appendix.

The author is deeply grateful to Mrs. Lily Yang for her assistance in the preparation of this manuscript.

2. LAMINAR HEAT TRANSFER—COLD WALL

In this section, analytic solutions are derived for the laminar boundary layer heating of surfaces with and without pressure gradients. Air will be treated as a real gas in equilibrium and continuum flow is assumed. However, the changes in heating that occur in low-density flows will be discussed.

2.1 Boundary Layer Equations

The boundary layer equations are written in the usual form, which assumes that the thickness of the layer is small compared to the body's radius of curvature and that centrifugal forces can be neglected. Following the historic development of references 1 and 2, the equations are further simplified by assuming a binary mixture of "air molecules" (instead of nitrogen and oxygen) and "air atoms" in thermodynamic equilibrium. (The binary gas mixture assumption greatly simplified the computation and was initially justified because the final results agreed well with experiments. Subsequently, it was computationally validated by Moss (ref. 11).) The expressions for the conservation of mass, momentum in the x and y directions, and energy are (ref. 4)

$$\frac{\partial}{\partial x}(\rho u r^j) + \frac{\partial}{\partial y}(\rho v r^j) = 0 \tag{1}$$

$$\rho u \frac{\partial u}{\partial x} + \rho v \frac{\partial u}{\partial y} = \rho_e u_e \frac{du_e}{dx} + \frac{\partial}{\partial y}\left(\mu \frac{\partial u}{\partial y}\right) \tag{2}$$

$$\rho u \frac{\partial w}{\partial x} + \rho v \frac{\partial w}{\partial y} = \frac{\partial}{\partial y}\left(\mu \frac{dw}{\partial y}\right) \quad \text{and} \quad \frac{\partial p}{\partial z} = 0 \tag{3}$$

$$\frac{\partial p}{\partial y} = 0 \tag{4}$$

$$\rho u \frac{\partial H}{\partial x} + \rho v \frac{\partial H}{\partial y} = \frac{\partial}{\partial y}\left[\frac{\mu}{Pr_f}(1 + F)\frac{\partial H}{\partial y} + \frac{\mu}{Pr_f} \times (Pr_f - 1 - F)\left(u \frac{\partial u}{\partial y} + w \frac{\partial w}{\partial y}\right)\right] \tag{5}$$

The coordinate systems are shown in figure 1. For a three-dimensional body of revolution, $j = 1$ and the velocity component $w = 0$. For a two-dimensional, infinite, yawed cylinder, $j = 0$, $w = w_e = \text{constant}$ and $\partial w/\partial z = 0$ in the boundary layer.

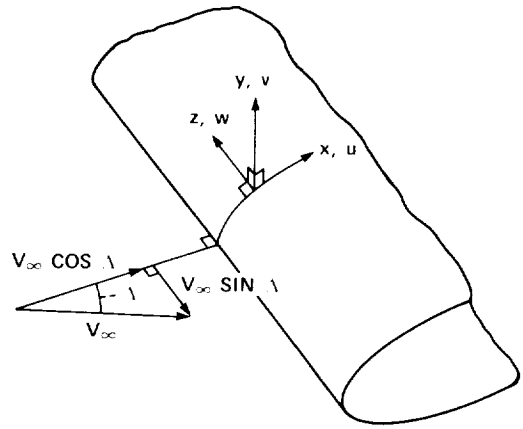

(a) COORDINATES FOR THE YAWED INFINITE CYLINDER

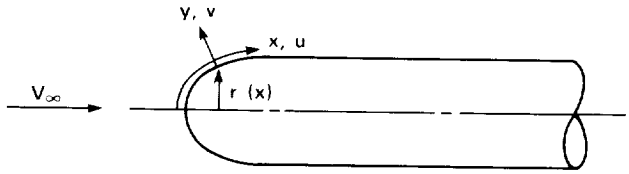

(b) COORDINATES FOR THE BODY OF REVOLUTION

Figure 1.– Boundary-layer coordinate systems.

For a binary gas mixture in thermodynamic equilibrium, the continuity equation does not have to be written for the individual species because the species concentrations are uniquely determined by the pressure and enthalpy, or any other two state properties. In the energy equation, the diffusion function, F, is defined as

$$F(p,h) = (Le - 1)(h_A - h_M)\left(\frac{\partial C_A}{\partial h}\right)_{p=\text{const.}} \tag{6}$$

The boundary conditions for the conservation relations, equation (1-5), are

at $y = 0$

$$u = v = w = 0$$
$$H = H_w(x) \tag{7}$$

and at the boundary layer edge

$$u = u_e(x) \quad \text{and} \quad w = w_e = \text{const.}$$
$$H = H_e = \text{const.} \tag{8}$$

The momentum and energy equations, equations (3) and (5), respectively, are now transformed to modified Lees similarity coordinates (refs. 1 and 2) by letting

$$\xi(x) = \frac{1}{\mu_0^2}\int_0^x \rho_w \mu_w u_e \left(\frac{r}{L}\right)^{2j} dx \tag{9}$$

and

$$\eta(x,y) = \frac{u_e (r/L)^j}{\mu_0\sqrt{2(\xi - \bar{\xi})}}\int_0^y \rho\, dy \tag{10}$$

where μ_0 is a reference value of the coefficient of viscosity, and $\bar{\xi}$ is a function of x, as yet undetermined. To satisfy continuity, equation (1), the stream function is introduced

$$\frac{\partial \psi}{\partial y} = \rho u \left(\frac{r}{L}\right)^j \tag{11a}$$

$$\frac{\partial \psi}{\partial x} = -\rho v \left(\frac{r}{L}\right)^j \tag{11b}$$

Combining equations (10) and (11a) gives

$$\frac{\partial \psi}{\partial \eta} = \mu_0\sqrt{2(\xi - \bar{\xi})}\left(\frac{u}{u_e}\right) \tag{12}$$

Now a new dependent variable can be defined as

$$f(x,h) = \frac{\psi}{\mu_0\sqrt{2(\xi - \bar{\xi})}} \tag{13}$$

where the velocity profile is given by

$$\frac{\partial f}{\partial \eta} = \frac{u}{u_e} \tag{14}$$

Writing the nondimensional spanwise velocity and enthalpy ratio, respectively, as

$$\zeta(\xi,\eta) = \frac{w}{w_e} \tag{15}$$

$$g(\xi,\eta) = \frac{H}{H_e} \tag{16}$$

and the ratio of the products of density and viscosity as

$$\varphi = \frac{\rho\mu}{\rho_e\mu_e} \tag{17}$$

permits transforming equations (2), (3) and (5) into the similarity coordinate systems. Now the momentum and energy equations become, respectively,

$$\frac{\partial}{\partial\eta}\left(\varphi\frac{\partial^2 f}{\partial\eta^2}\right) + \left(1 - \frac{d\bar{\xi}}{d\xi}\right) f\frac{\partial^2 f}{\partial\eta^2} = \beta\left[\left(\frac{\partial f}{\partial\eta}\right)^2 - \frac{g}{t_s} + \left(\frac{1 - t_s}{t_s}\right)\zeta^2 - \frac{t_e}{t_s}\left(\frac{\rho_e}{\rho} - \frac{t}{t_e}\right)\right] + 2(\xi - \bar{\xi})\left(\frac{\partial f}{\partial\eta}\frac{\partial^2 f}{\partial\eta\partial\xi} - \frac{\partial f}{\partial\xi}\frac{\partial^2 f}{\partial\eta^2}\right) \tag{18}$$

$$\frac{\partial}{\partial\eta}\left(\varphi\frac{\partial\zeta}{\partial\eta}\right) + \left(1 - \frac{d\bar{\xi}}{d\xi}\right) f\left(\frac{\partial\zeta}{\partial\eta}\right) = 2(\xi - \bar{\xi})\left(\frac{\partial f}{\partial\eta}\frac{\partial\zeta}{\partial\xi} - \frac{\partial f}{\partial\xi}\frac{\partial\zeta}{\partial\eta}\right) \tag{19}$$

$$\frac{\partial}{\partial\eta}\left[\frac{\varphi}{Pr_f}(1 + F)\frac{\partial g}{\partial\eta}\right] + \left(1 - \frac{d\bar{\xi}}{d\xi}\right) f\left(\frac{\partial g}{\partial\eta}\right) = \frac{\partial}{\partial\eta}\left\{\frac{\varphi}{Pr_f}(1 - Pr_f + F) \times\left[(t_s - t_e)\frac{\partial}{\partial\eta}\left(\frac{\partial f}{\partial\eta}\right)^2 + (1 - t_s)\frac{\partial}{\partial\eta}(\zeta^2)\right]\right\} + 2(\xi - \bar{\xi})\left(\frac{\partial f}{\partial\eta}\frac{\partial g}{\partial\xi} - \frac{\partial f}{\partial\xi}\frac{\partial g}{\partial\eta}\right) \tag{20}$$

where the pressure gradient parameter, β, is defined as

$$\beta = \frac{2(\xi - \bar{\xi})}{u_e}\frac{t_s}{t_e}\frac{du_e}{d\xi} \tag{21}$$

and the ratio of static to total enthalpy is

$$t = \frac{h}{H_e} = g - (1 - t_s)\zeta^2 - (t_s - t_e)\left(\frac{\partial f}{\partial\eta}\right)^2 \tag{22}$$

For the body of revolution at $\alpha = 0$, $t_s = 1$ and $\zeta = 0$. On the infinite yawed cylinder, t_s is constant and given by

$$t_s = 1 - \frac{w_e^2}{2H_e} = 1 - \frac{V_\infty^2 \sin^2\Lambda}{2H_e} \tag{23}$$

which is the static enthalpy ratio at the boundary layer edge along the stagnation line. The boundary conditions in the similarity coordinate system for equations (18)-(20) are at $\eta = 0$ (wall)

$$f(0,\xi) = \frac{\partial f}{\partial \eta}(0,\xi) = \zeta(0,\xi) = 0 \tag{24a}$$

$$g(0,\xi) = g_w(\xi) = t_w(\xi) \tag{24b}$$

as $\eta \rightarrow \infty$ (boundary layer edge)

$$\frac{\partial f}{\partial \eta}(\infty,\xi) = \zeta(\infty,\xi) = g(\infty,\xi) = 1 \tag{25}$$

2.2 Similar Solutions

Partial differential equations were traditionally difficult to solve numerically. However, when written in the local similarity coordinates, the equations can be readily solved numerically. Exact solutions can also be found for a (limited) number of conditions where the flow external to the boundary layer and the wall temperature became independent of the streamline coordinate $\xi(x)$.Practical examples of such exact similar solutions are the flow at a three-dimensional stagnation point, at the stagnation line on a two-dimensional infinite cylinder, and on an inclined sharp flat plate or a sharp cone having a constant wall temperature. For the preceding conditions, the partial differential equations become ordinary differential equations, which are much easier to solve.

Most practical problems of interest, however, do not have exact solutions. A widely used approximation is to assume that such flows can be treated as if they were locally similar. The procedure consists of assuming that the derivatives with respect to $\xi(x)$ vary relatively slowly and can be neglected, while the local values are used for the terms which depend on $\xi(x)$ through the external flow or the wall conditions. Again, a set of ordinary differential equations results which can be solved for the required boundary layer profiles. The solutions thus found are then applied at each value of $\xi(x)$ in the nonsimilar flow by using the approximate values of t_s and the local values of t_e, g_w, and β. Under the local similarity conditions, the value of $d\xi/d\xi$ becomes arbitrary and may be set equal to zero (ref. 3). The momentum and energy equations, equations (18)-(20), can now be written as ordinary differential equations, where primes denote differentiation with respect to η, to yield

$$(\varphi f'')' + ff'' = \beta\left[(f')^2 - \frac{g}{t_s} + \left(\frac{1 - t_s}{t_s}\right)\zeta^2 - \frac{t_e}{t_s}\left(\frac{\rho_e}{\rho} - \frac{t}{t_e}\right)\right] \tag{26}$$

$$(\varphi\zeta')' + f\zeta' = 0 \tag{27}$$

$$\left[\frac{\varphi}{Pr_f}(1 + F)g'\right]' + fg' = \left\{\frac{\varphi}{Pr_f}(1 - Pr_f + F) \times \left[(t_s - t_e)(f')'^2 + (1 - t_s)(\zeta^2)'\right]\right\}' \tag{28}$$

The boundary conditions are

$$f(0) = f'(0) = \zeta(0) = 0 \tag{29a}$$

$$g(0) = g_w \tag{29b}$$

while the parameters β, t_s, t_e, and g_w are evaluated locally along the body. The similar boundary layer equations can be numerically integrated in a straightforward manner for high-speed flight conditions if the high-temperature thermodynamic and transport properties are known.

2.3 Thermodynamic and Transport Properties

In 1958, the first set of high-temperature thermodynamic (ref. 5) and transport (ref. 6) properties for air became widely available and were extensively used for the following two decades. Although more precisely calculated values for the transport properties were published in the early 1960s by Peng and Pindroh (ref. 12) and Yos (ref. 13), the reports were not widely circulated. In references 14-16, the transport properties from references 6, 12, and 13 were compared and it was shown that Hansen's coefficients of viscosity and thermal conductivity were too low at temperatures above 2000 K. While such inaccuracies should not be ignored, it was shown by Howe and Sheaffer (ref. 17) that varying the coefficient of thermal conductivity by a factor of 10 resulted in a 40% increase in the stagnation point heating rate at a speed of about 18 km/sec.

For use with computer codes, the analytic approximations for high-temperature air properties developed by Worbs and Bolster (ref. 18) are useful. When fast computers are available, the program of Gordon and McBride (ref. 19) can be used as a subroutine and gives thermodynamic properties and species concentrations to 6000 K that compare closely with those of reference 5.

2.4 Heat Transfer Rate at a Stagnation Point or Line

The general expression for the heat transfer rate to the wall can be written (ref. 4)

$$\dot{q}_w = \frac{\mu_w}{Pr_{wf}}(1 + F_w)\left(\frac{\partial h}{\partial y}\right)_w \tag{30a}$$

or, in the similar coordinate system

$$\dot{q}_w = \frac{H_e}{Pr_{wf}}(1 + F_w)g'_w \left(\frac{\rho_w \mu_w t_s}{\beta t_e}\frac{du_e}{dx}\right)^{0.5} \quad (30b)$$

The dimensionless heat transfer parameter consisting of Nusselt number and Reynolds number, evaluated using static wall conditions, can be written as

$$\frac{Nu_w}{(Re_w)^{0.5}} = \frac{g'_w}{g_{aw} - g_w}(1 + F)\left(\frac{t_s}{\beta t_e}\frac{x}{u_e}\frac{du_e}{dx}\right)^{0.5} \quad (31)$$

where

$$g_{aw} = t_e + \bar{r}(1 - t_e)$$

and $\bar{r}$ is the recovery factor. Two exact solutions to equations (26)-(28) consisting of the axisymmetric stagnation point and the stagnation line on a yawed, infinite cylinder will be presented next. The equations were numerically integrated using references 5 and 6. The calculations were performed to temperatures up to the onset of ionization, which corresponds to a flight speed of almost 9 km/sec. A unit Lewis number was used so that $F = 0$; this assumption can introduce errors of up to 8% in the heating rate (ref. 4).

For the axisymmetric stagnation point $j = 1$, $\beta = 0.5$, $t_s = t_e = 1$ and $du_e/dx = u_e/x$, so that equation (31) gives

$$\frac{Nu_w}{(Re_w)^{0.5}} = \frac{\sqrt{2}\, g'_w}{1 - g_w}(1 + F)$$

For a recovery factor, $\bar{r}$, of 0.85 and

$$\left(\frac{\rho_e \mu_e}{\rho_w \mu_w}\right)_s \leq 1$$

Reference 4 gives the expression

$$\frac{Nu_w}{(Re_w)^{0.5}} = 0.57 Pr_{wf}^{0.4}\left(\frac{\rho_e \mu_e}{\rho_w \mu_w}\right)_s^{0.45} \quad (36a)$$

and for

$$\left(\frac{\rho_e \mu_e}{\rho_w \mu_w}\right) \geq 1$$

$$\frac{Nu_w}{(Re_w)^{0.5}} = 0.57 Pr_{wf}^{0.4}\left(\frac{\rho_e \mu_e}{\rho_w \mu_w}\right)_s^{0.67} \quad (36b)$$

where equation (36b) is applicable for large yaw angles and highly cooled walls. Note that for

$$\left(\frac{\rho_e \mu_e}{\rho_w \mu_w}\right)_s = 1$$

Correlation of the numerical calculations yields (ref. 4)

$$\frac{Nu_w}{(Re_w)^{0.5}} = 0.767 Pr_{wf}^{0.4}\left(\frac{\rho_e \mu_e}{\rho_w \mu_w}\right)_s^{0.43} \quad (32)$$

which can be compared to the expression from reference 2 of

$$\frac{Nu_w}{(Re_w)^{0.5}} = 0.768 Pr_{wf}^{0.4}\left(\frac{\rho_e \mu_e}{\rho_w \mu_w}\right)_s^{0.40} \quad (33)$$

Using equation (32) yields the heat transfer rate

$$\dot{q}_{ws} = \frac{0.767}{Pr_{wf}^{0.4}}(H_e - h_w)_s(\rho_e \mu_e)^{0.43}(\rho_w \mu_w)^{0.07}\left(\frac{du_e}{dx}\right)_s^{0.5} \quad (34)$$

For the yawed, infinite cylinder $j = 0$, $\beta = 1$, $t_s = t_e \leq 1$, and $du_e/dx = u_e/x$ so that

$$\frac{Nu_w}{(Re_w)^{0.5}} = \frac{g'_w}{g_{aw} - g_w}(1 + F_w) \quad (35)$$

the ratio of equation (32) to equation (36a) disagrees by only 5% from the theoretical value of $2^{-0.5}$, which relates the stagnation heating rates on an axisymmetric body and a cylinder.

The usefulness of the correlation equations are further improved by writing the relations directly in terms of flight condition. Examples of such correlations are shown in figure 2 for the laminar heat transfer parameter for the stagnation point on a hemisphere, an unswept circular cylinder, sharp cones, and a sharp flat plate. (A wall temperature of 300 K was used for the calculations illustrated in figure 2 to facilitate comparison with shock tube data.) Note that the maximum difference between the four hemispherical stagnation point calculations (refs. 2 and 20-22) is about 15% and can, partly, be attributed to using different high-temperature transport properties. The sharp cone values (refs. 23 and 24) differ by 8% at low speeds and much less at high speeds.

The calculations shown as straight lines in figure 2 can be used to derive simple analytic approximations for the heat transfer rate. Noting that

$$\frac{Nu_w}{(Re_w)^{0.5}} = \frac{C_1 T_w^b}{V_\infty^a} \quad (37)$$

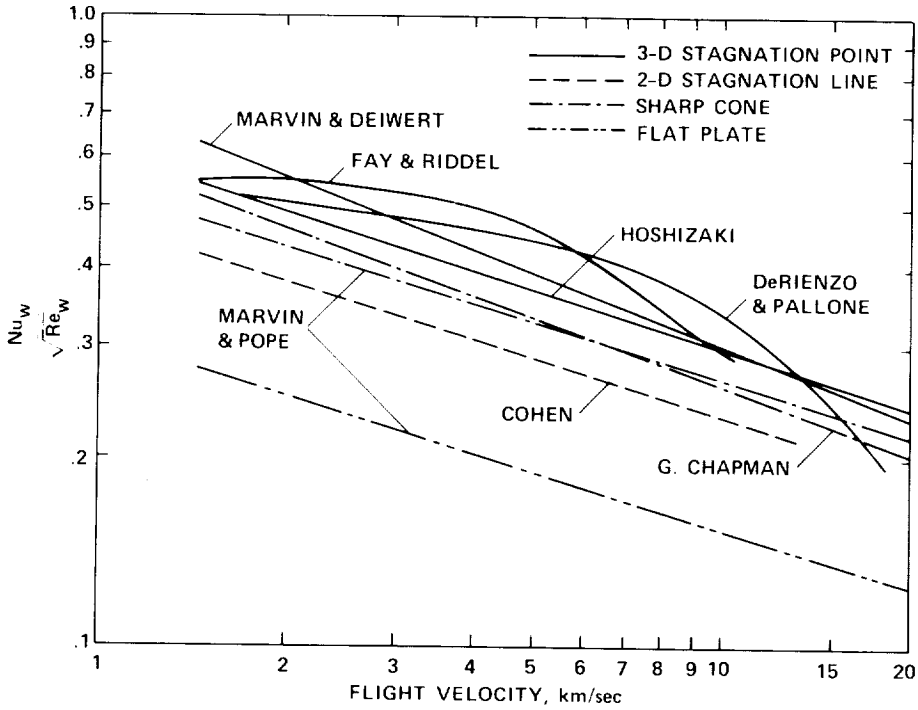

Figure 2.– Comparison of laminar convective heat-transfer parameter calculations.

where the exponent "a" varies from 0.3 to 0.4, "b" varies from 0.10 to 0.20, and C_1 is a constant, and substituting the expressions for Nusselt and Reynolds number, yields the axisymmetric stagnation point heat transfer rate

$$\dot{q}_{w_S} = \left[\frac{C_1 T_w^b}{Pr_w}\left(\frac{\mu_w}{RT_w Z_w}\right)^{0.5}\right]\left(\frac{V_\infty^2}{2} + h_\infty - h_w\right)V_\infty^{-a}$$

$$\times p_s^{0.5}\left(\frac{du_e}{dx}\right)_s^{0.5} \qquad (38)$$

where p_S is the stagnation pressure. The velocity gradient at a hemispherical stagnation point can be evaluated using Newtonian theory (ref. 2), which gives

$$\left(\frac{du_e}{dx}\right)_s = \frac{1}{r_n}\left[\frac{2(p_s - p_\infty)}{\rho_s}\right]^{0.5} \qquad (39a)$$

where

$$p_S = \rho_\infty V_\infty^2\left(1 - \frac{\varepsilon}{2}\right) + p_\infty$$

and $\varepsilon = \rho_\infty/\rho_S$. At high speeds $\varepsilon << 1$, and

$$\left(\frac{du_e}{dx}\right)_s \approx \frac{V_\infty}{r_n}(2\varepsilon)^{0.5} \qquad (39b)$$

An empirical expression for ε which is valid within about ±10% in the speed range from 10^3 m/sec to 10^4 m/sec, is

$$\varepsilon \approx 11.4 V_\infty^{-0.57} \qquad (39c)$$

For wall temperatures of less than about 4000 K, the Prandtl number variation is small and the coefficient of viscosity can be approximated by

$$\mu_w \sim T_w^{0.71}$$

If the exponent, b, in equation (37) is set equal to 0.145, then the bracket in equation (38) becomes independent of wall temperature. Using a value for the exponent, a, of 0.3575, and if the flight speed is high enough so that $h_\infty << V_\infty^2/2$, one can now write equation (38) in the simple and useful form

$$\dot{q}_{w_S} \approx 1.83(10^{-4})\left(\frac{\rho_\infty}{r_n}\right)^{0.5} V_\infty^3\left(1 - \frac{h_w}{H_S}\right) \quad \frac{W}{m^2} \qquad (40)$$

where the nose radius, r_n, is in m, the free-stream density is in kg/m^3, and the flight velocity is in m/sec. The correlation equation for air given by Marvin and Deiwert (ref. 21) is nearly the same as equation (40). (Stagnation point heating correlations in gases other than air are given in refs. 21 and 25.) The analogous expression for the swept, infinite cylinder is

$$\dot{q}_{w_{cyl}} \approx 1.29(10^{-4})\left(\frac{\rho_\infty}{r_{cyl}}\right)^{0.5}(1 - 0.18\sin^2\Lambda)V_\infty^3$$

$$\times\left(1 - \frac{h_w}{h_{aw}}\right)\cos\Lambda \qquad \frac{W}{m^2} \quad (41)$$

where

$$h_{aw} \approx h_\infty + 0.5V_\infty^2(1 - 0.18\sin^2\Lambda)$$

and Λ is the sweepback angle. In writing equation (41) it has been implicitly assumed that the stagnation point velocity gradients are identical for the sphere and cylinder. According to reference 8, the Newtonian value, equation (39), is accurate for the circular cylinder, but 7.7% too low for the sphere. If the velocity gradient value of reference 8 were used in equation (40), the constant would increase from 1.83 to 1.90.

A comparison with experimental data is shown in figure 3 for the four hemispherical stagnation point correlations of figure 2. Up to a speed of 14 km/sec, all four correlations, from references 2 and 20-22, lie within the data spread, which is about ±25%. In addition to the shock tube data, five measurements based on observations of the onset of melting of projectiles fired in a ballistic range by Compton (ref. 26) are also shown. The ballistic range data confirm the shock tube measurements and theories of references 20 and 21 in the low ionization velocity regime. At speeds above 14 km/sec where ionization effects are very strong, Hoshizaki's formulation (ref. 20) appears to give the best agreement with the data of Rose and Stankevics (ref. 27). The strong ionization regime is also characterized by intense radiative heating, which can be much greater than the convective heating.

Newtonian theory, equation (39), can be used to predict the velocity gradients reasonably well on circular cylinders and hemispheres. However, for blunter configurations more precise numerical methods, or experimentally derived values, must be used. In figure 4, a comparison between experimentally determined velocity gradients and values calculated using Newtonian theory shows the limitations of the Newtonian approximation for determining stagnation point velocity gradients on blunt bodies.

2.5 Blunt-Body Heating-Rate Distributions

The distribution of the heat-transfer rate around a blunt-nosed axisymmetric body, or a yawed cylinder, can be determined using the local boundary layer similarity approximation. Following reference 4, the ratio of the local heat transfer to the stagnation value is written as

$$\frac{\dot{q}_w}{\dot{q}_{w_S}} = \left[\left(\frac{\rho_w\mu_w}{\beta t_e}\frac{du_e}{dx}\right) \Big/ \left(\frac{\rho_w\mu_w}{\beta t_e}\frac{du_e}{dx}\right)_s\right]^{0.5} \Gamma \quad (42)$$

where the velocity gradient parameter, β, is

$$\beta = \frac{2t_S(du_e/dx)}{\rho_w\mu_w u_e^2 t_e (r/L)^{2j}\Gamma^2}\int_0^x \rho_w\mu_w u_e\left(\frac{r}{L}\right)^{2j}\Gamma^2\,dx \quad (43)$$

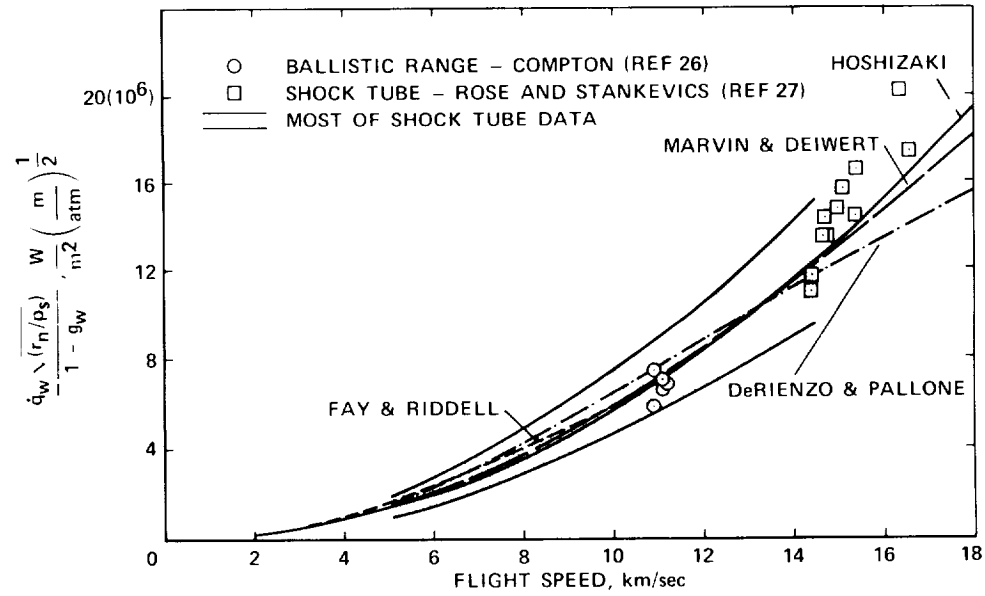

Figure 3.– Stagnation point convective heating comparisons.

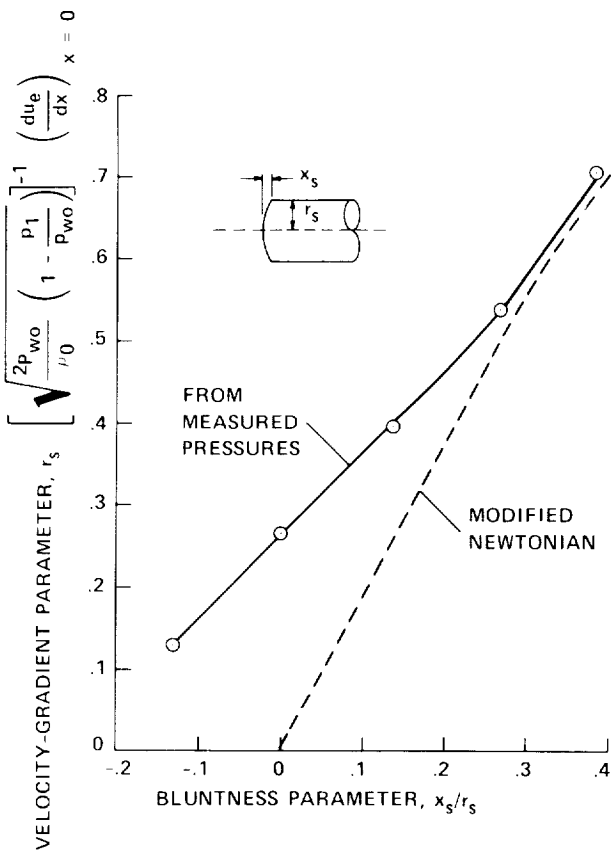

Figure 4.– Stagnation-point velocity gradient variation with body bluntness at Mach 4.76.

and

$$\Gamma = \left(\frac{1 + F_w}{Pr_w}\right) g'_w \Big/ \left(\frac{1 + F_w}{Pr_w}\right)_s g'_{w_s}$$

The gradient of the enthalpy ratio at the wall, g'_w, is determined by solving the locally similar boundary layer equations (26)-(28). The full solution of Eqs. (42) and (43) requires iterating, because Γ is inside the integral in Eq. (43). However, it is consistent with the local similarity assumption to set $\Gamma = 1$ in Eq. (43), thus eliminating the iteration. The result is essentially the same as that of Kemp et al. (ref. 28) and is shown in figure 5 for a hemisphere and figure 6 for a circular cylinder. Also illustrated in figures 5 and 6 is the solution of reference 1, which results when $\Gamma = 1$ in both Eq. (42) and (43). For the axisymmetric body, numerical solutions were correlated to yield

$$\frac{\dot{q}_w}{\dot{q}_{w_s}}\left[2\rho_w\mu_w\left(\frac{du_e}{dx}\right)\right]_s^{0.5}\frac{\mu_0 L(2\xi)^{0.5}}{\rho_w\mu_w u_e r} = \frac{1 + 0.096(\beta t_e)^{0.5}}{1.068} \qquad (44)$$

for a Lewis number of one and $g_w << 1$.

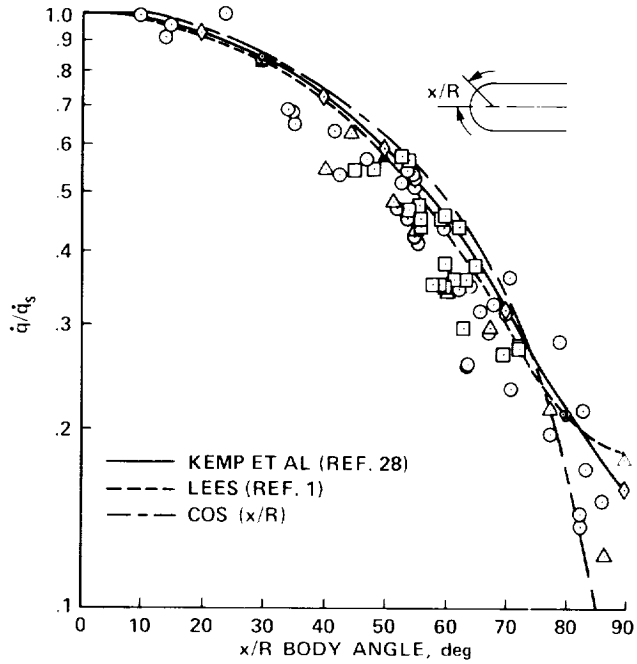

Figure 5.– Heat-transfer distribution on hemisphere cylinder. (From ref. 28; reprinted with permission of The American Institute of Aeronautics and Astronautics.)

Also shown in figures 5 and 6 are heating solutions following a cosine variation of the body angle measured from the stagnation point. Although it is approximate, the cosine variation of heating has a theoretical basis (ref. 1) at least to the body sonic point (near 45°) and appears to give reasonable results to about 70° beyond the stagnation point.

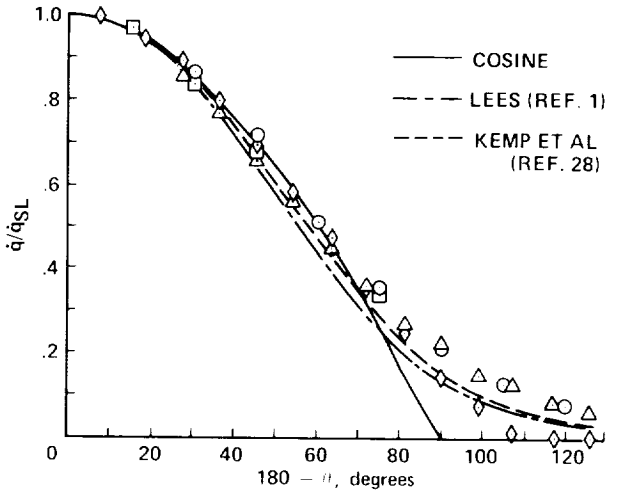

Figure 6.– Comparison of predicted and measured heat flux distributions on a circular cylinder normal to a stream.

The local similarity solution procedure has also been applied to a blunt-faced axisymmetric body with a small corner radius. The results of using the methods of references 1 and 28 to calculate the heating distribution are illustrated in figure 7. Again, the method of reference 28 is

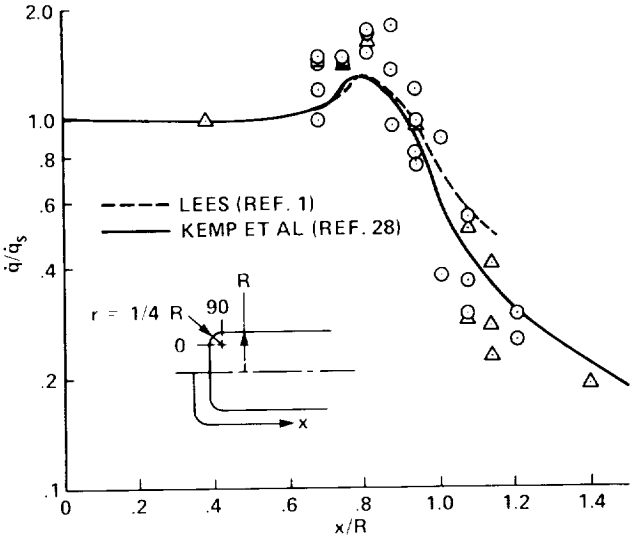

Figure 7.– Heat-transfer distribution on flat-nosed body. (From ref. 28; reprinted with permission of The American Institute of Aeronautics and Astronautics.)

seen to give somewhat better results than that of reference 1, although there is much scatter in the data.

2.6 Cone and Flat Plate Heating Rates

The laminar boundary layer heating of bodies without pressure gradients ($\beta = du_e/dx = 0$) such as sharp cones and flat plates at angle of attack will now be considered. The expression for the heating rate on a sharp cone in air is, from reference 23, after noting that the total enthalpy term should be replaced by the recovery enthalpy,

$$\dot{q}_{w_c} = \frac{0.018}{Pr_w}\left(\frac{\rho_e u_e}{x}\right)^{0.5} h_{aw}^{0.85}\left(1 - \frac{h_w}{h_{aw}}\right) \quad \frac{W}{m^2} \quad (45)$$

where ρ_e is in atm, u_e is in m/sec, x is in m, and h is in m^2/sec^2. At high speeds, where $h_\infty << V_\infty^2/2$, and using the Newtonian flow approximation

$$\rho_e u_e \approx \rho_\infty V_\infty^3 \sin^2 \delta_c \cos \delta_c$$

and the transport properties of reference 15, equation (45) becomes

$$\dot{q}_{w_c} \approx 4.03(10^{-5})\left(\frac{\rho_\infty \cos \delta_c}{x}\right)^{0.5}$$

$$\times V_\infty^{3.2} \sin \delta_c \left(1 - \frac{h_w}{h_{aw}}\right) \quad \frac{W}{m^2} \quad (46)$$

where

$$h_{aw} \approx h_\infty + 0.40V_\infty^2$$

and δ_c is the cone half angle. In practice, all cones have some tip bluntness. Usually, the nose blunting will reduce the heating on the cone surface aft of the nose. In an analysis made for a perfect gas of $\gamma = 1.4$, Vallerani (ref. 29) showed that the local heating is reduced at a flight Mach number of 5, or greater, for $5° < \delta_c < 25°$, but increased for larger half-cone angles.

The sharp wedge, or inclined flat plate, heating rates can be found from equation (45) by using the Mangler transformation which is

$$\dot{q}_{wFP} = \dot{q}_{w_c}/(3)^{0.5} \quad (47)$$

However, the Newtonian approximation for $\rho_e u_e$ is not as accurate for a wedge as for a cone. After adjusting the Newtonian values, an approximation for the inclined flat plate which is equivalent to equation (46) is

$$\dot{q}_{wFP} \approx 2.42(10^{-5})\left(\frac{\rho_\infty \cos \delta_{FP}}{x}\right)^{0.5}$$

$$\times V_\infty^{3.2} \sin \delta_{FP}\left(1 - \frac{h_w}{h_{aw}}\right) \quad \frac{W}{m^2} \quad (48)$$

where δ_{FP} is the wedge angle, or angle of attack of the plate.

2.7 Wing Leading-Edge Heating

The heating along a cylindrical leading edge of a finite-length wing can be approximately calculated using the expression of Rubesin (ref. 30)

$$\dot{q}_{wLE} \approx \left(\dot{q}_{w_{cyl}}^2 + \dot{q}_{wFP}^2 \sin^2 \Lambda\right)^{0.5} \cos \alpha \quad (49)$$

where $\dot{q}_{w_{cyl}}$ is given by equation (41) and q_{FP} by equation (48). For highly swept leading edges, equation (49) is limited to small angles of attack, since the stagnation line moves from the cylindrical leading edge onto the lower surface of the wing as the angle of attack increases.

2.8 Low-Density Flow Heating

The peak hypersonic aerodynamic heating experienced by missiles or manned vehicles always occurs in the continuum flow regime. However, sometimes vehicles have small nose or wing leading-edge radii, and these regions of the vehicle can experience low-density flow phenomena which alter the heating. For example, if a vehicle flying at high altitude has a small nose radius, the Reynolds number on the nose ceases to be large. In that case, the basic assumptions of the Prandtl boundary layer theory are violated as the boundary layer becomes thick and slip can occur at the body surface. In addition, shock waves can become

thick, or diffuse, and occupy a significant fraction of the shock layer. The low-density flow field and heating are discussed by Shorenstein and Probstein (ref. 31) and Shorenstein (ref. 32) for flat plates and cones. Axisymmetric stagnation point heating measurements are presented and compared with theory by Boylan (ref. 33). One parameter that characterizes low-density flows is the Knudsen number, which is the ratio of molecular mean free path to body size. The increase in stagnation point heat transfer coefficient with Knudsen number and altitude was calculated by Moss et al. (ref. 34) and is shown in figure 8. For a nose radius of 2.54 cm, the heat-transfer coefficient, predicted by the direct simulation Monte Carlo (DSMC) method, increases tenfold in the altitude range of 60-100 km. Of course, the heat-transfer rate decreases by two orders of magnitude because of the atmospheric density decrease with altitude. From figure 8, it is also evident that neglecting slip at the wall can lead to a 130% overprediction of the heating at a Knudsen number of 0.1. (The results from DSMC methods have been verified by comparison with experimental data by Nomura (ref. 35).)

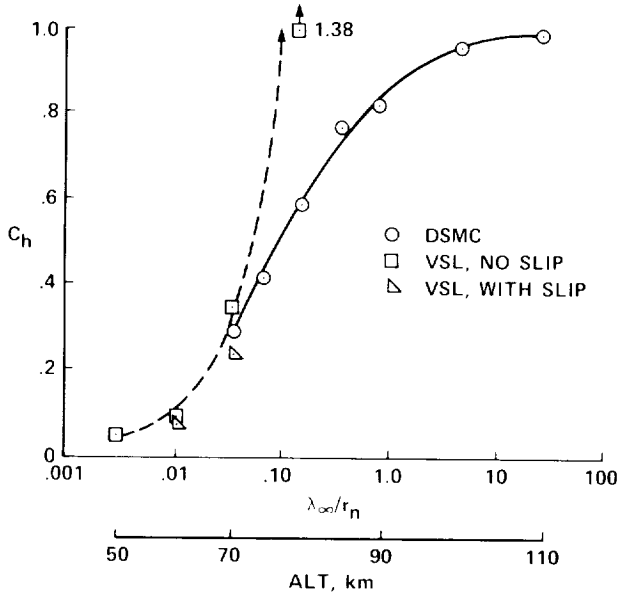

Figure 8.– Stagnation-point heat-transfer coefficient versus Knudsen number. V_∞ = 7.5 km/sec, r_n = 2.54 cm. (From ref. 34.)

This concludes the discussion of cold-wall laminar heat transfer. Next, boundary layer transition will be briefly covered.

3. BOUNDARY LAYER TRANSITION

The transition of the boundary layer from laminar to turbulent flow remains the most complex problem in fluid mechanics. At hypersonic speeds, turbulent boundary layer heating can be several times greater than laminar heating. Therefore, it is essential that some form of reliable means of predicting transition be available to avoid the penalties that result from overly conservative design. Because transition is influenced by many factors, the engineer must rely on empirical relations derived from test data. However, none of the ground test facilities can simulate most of the parameters of interest; in fact, the operating characteristics of many test facilities have been found to strongly influence the data. In the following sections, some examples of test data will be discussed and a few correlation charts and formulas from the open literature will be presented.

It has long been known that among the important parameters influencing transition are the boundary layer edge Reynolds number and Mach number. The results of plotting measurements of the Reynolds number calculated at the beginning of transition against Mach number are illustrated in figure 9 for flow on cones. At first glance, figure 9 appears to be a shotgun pattern of data points, with transition Reynolds numbers varying from about 1 million to 30 million. However, even within this jumble of data there are some definite trends. First, note that the flight data give the highest transition Reynolds numbers and the wind tunnel data give the lowest values. The ballistic range points fall, more or less, in the middle. The tendency to predict early transition in many wind tunnels has been widely observed (refs. 36 and 37) and correlated by Dougherty and Fisher (ref. 37) with the intensity and, to some extent, the frequency of the disturbances in the facilities. The problems encountered in wind tunnel test measurements of transition have encouraged the use of ballistic ranges (ref. 38 and 39). More recently, the development and use by Beckwith (ref. 40) of a low-disturbance, high Reynolds number, supersonic wind tunnel has yielded valuable data (refs. 41 and 42). For example, Chen et al. (ref. 42) measured similar transition Reynolds numbers at a Mach number of 3.5, on flat plates and slender cones with adiabatic walls. In high-noise wind tunnel tests, the transition Reynolds numbers on flat plates were only half as large as the values measured on cones (ref. 42), implying that the flat-plate boundary layer was more sensitive to free-stream disturbances.

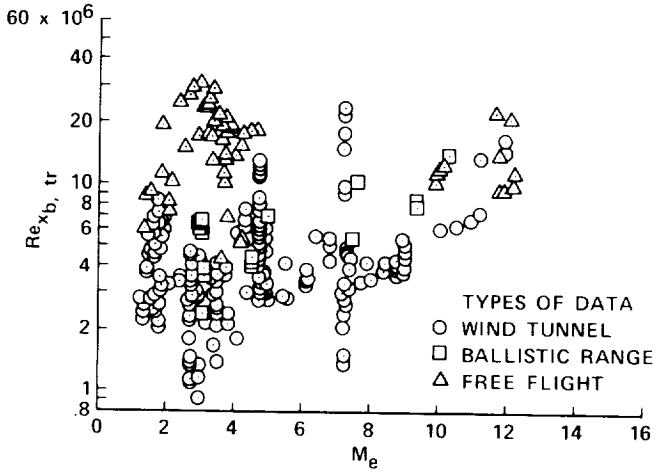

Figure 9.– Typical transition data—cones.

Some empirical correlations for the beginning of transition found in the open literature will now be discussed. Despite the data scatter in figure 9, there is a discernible trend of increasing transition Reynolds number with rising Mach number. The same trend was observed by Softley et al. (ref. 43) and is shown in figure 10 (taken from ref. 43).The data in figure 10 are for sharp cones, having Reynolds numbers based on nose radii of less than 200. The high stability of the laminar boundary layer to disturbances at hypersonic edge Mach numbers has been observed by other researchers (ref. 44) and lends credence to the trend shown in figure 10. However, the influence of wall temperature on hypersonic transition appears to be an open issue, with some tests showing strong effects and other tests indicating little effect (ref. 43).

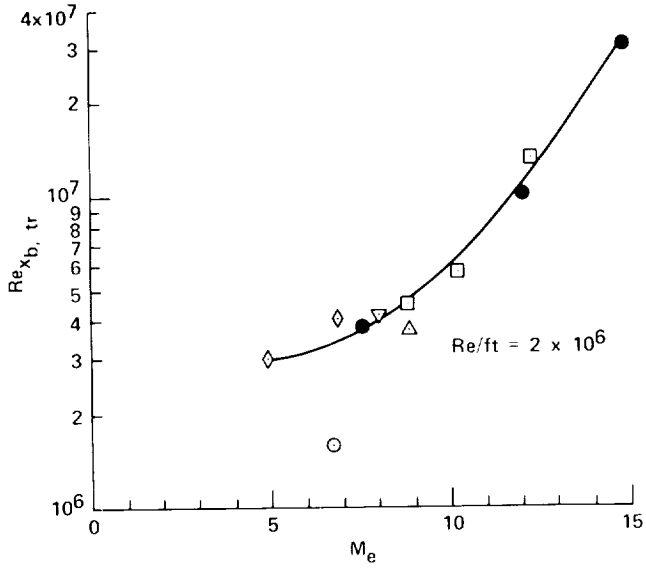

Figure 10.– Effect of local Mach number on transition Reynolds number—sharp slender cones—uniform wall temperature. (From ref. 43; reprinted with permission of The American Institute of Aeronautics and Astronautics.)

Unlike the hypersonic boundary layer, the subsonic one existing on the blunt noses of high-speed flight vehicles is easily tripped by surface roughness. The mechanism has been extensively studied and correlations have been published (refs. 45-47). Since strong pressure gradients exist on the blunt noses, the correlations are for Reynolds numbers based on boundary layer momentum thickness rather than the body lengths used for sharp cones and flat plates. A formula suggested by Laderman (ref. 46) is

$$Re_{\theta_{bt}} = 215 \Big/ \left(\frac{k}{\theta}\frac{T_c}{T_w}\right)^{0.7} \qquad (50)$$

where k/θ is the ratio of roughness element height to local momentum thickness. (Charts of momentum thickness in high-speed flight for bodies with various amounts of nose bluntness can be found in ref. 48.) Another correlation for surface-roughness-induced transition is presented by Amirkabirian et al. (ref. 49) for the Shuttle orbiter and is shown in figure 11. Although the Shuttle tiles are very smooth, the "roughness" results from misaligned tiles and the gaps between tiles. Again, most of the flight data points are well above the shaded band, which is based on wind-tunnel tests. An approximate correlation is (ref. 49)

$$Re_\theta/M_e = \text{const.} \qquad (51)$$

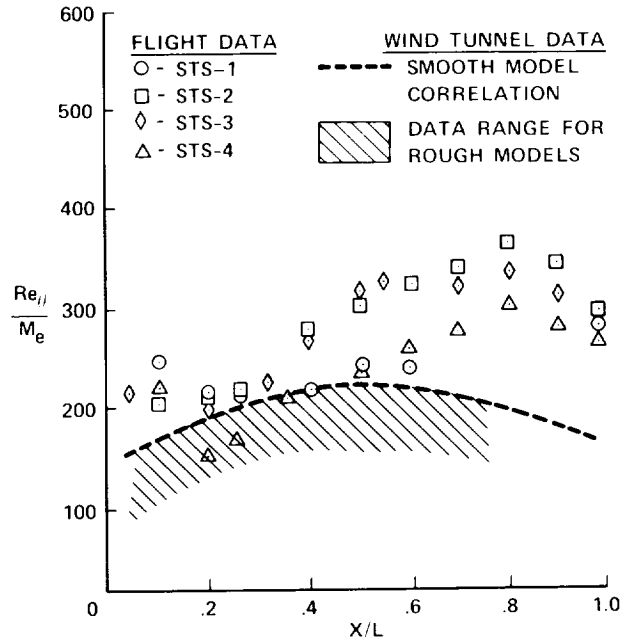

Figure 11.– Flight values of the transition parameters. (From ref. 49; reprinted with permission of The American Institute of Aeronautics and Astronautics.)

where the constant varies from 150 to 350, depending on the ratio of roughness height to momentum thickness, etc. Additional transition data are available for configurations of practical interest such as blunted cones at angle of attack (ref. 50) and on swept-wing leading edges (ref. 51). Despite the high-transition Reynolds numbers which can be expected at hypersonic speeds, full-sized vehicles will still experience turbulent boundary layers over much of their surface. The heat transfer resulting from turbulent boundary layers will be discussed next.

4. TURBULENT HEAT TRANSFER—COLD WALL

For the laminar boundary layer, it was shown that exact solutions could be found which model the viscous flow over important regions of a vehicle. In contrast with the laminar boundary layer, there is no complete theory for modeling the turbulent transport of mass, momentum, and energy. The equations for the turbulent boundary layer can be formulated only with the aid of experimental data such as mixing lengths, etc. Therefore, all turbulent "theories" are semi-empirical and care must be taken when these formulations

are applied beyond the range of conditions for which they were derived.

4.1 Comparison of Approximate Methods

A number of approximate methods have been widely used to calculate the turbulent boundary layer heating. All of the methods rely on Reynolds analogy which relates skin friction and heat transfer (ref. 8). In addition, all methods use some form of coordinate transformation for extending the well-verified incompressible skin-friction and heat-transfer formulas to the compressible, high-speed conditions. The transformations therefore are functions of Mach number, Reynolds numbers, and temperatures at the boundary layer edge and at the wall. Among the most widely used approaches are the reference enthalpy, or reference temperature, Spalding and Chi, Van Driest II, and Coles. These methods have been extensively compared and their formulations explained in the literature by Hopkins and Inouye (ref. 52) and by Cary and Bertram (ref. 53); therefore, only brief descriptions will be presented here.

The reference temperature concept was originated by Rubesin and Johnson (ref. 54) and the coefficients modified by Sommer and Short (ref. 55). The basic assumption is that a temperature within the boundary layer can be calculated, using an expression with empirically determined coefficients, which will yield the correct skin friction in a compressible, supersonic boundary layer when the incompressible relations are used. Although the method was first formulated for laminar boundary layers, it was found to give good results for turbulent boundary layers also. Eckert (ref. 56) extended the method to high-speed flows in equilibrium having real gas effects by using enthalpy in place of temperature. Van Driest II refers to Van Driest's second method which uses the von Karman mixing length (ref. 57). In addition, the Crocco temperature profile is assumed through the boundary layer. The Spalding and Chi method (ref. 58) uses Van Driest's formulation to relate the incompressible and compressible boundary layer skin friction. Empirical expressions are used containing the boundary layer edge, wall, and recovery temperatures. The correlation functions were empirically determined using a large body of data. However, some of the data contained systematic errors, yet all data were weighed equally. The method of Coles (ref. 59) is based on the concept of a constant mean temperature of a layer, called the substructure, which is located near the wall but extends beyond the laminar sublayer. The substructure temperature is based on the boundary layer edge Mach number and temperature and the wall temperature and is used to evaluate a Reynolds number. Additional mathematical details on the above four methods can also be found in reference 8.

The ability of the four methods to predict turbulent heat transfer has been compared by several authors. The comparisons of Hopkins and Inouye (ref. 52) are shown in figure 12 for the Mach number range 4.9 to 7.4 and for ratio of wall temperature to recovery temperature from 0.1 to 0.82. The conclusion drawn from figure 12 and comparisons in reference 52 is that the Van Driest II method gave the best overall results while Spalding-Chi consistently underpredicted the heating. However, note that disagreement between the prediction and the data of 20% to 30% is common. The conclusions of reference 52 are corroborated by the results of Chien (ref. 60) in figure 13 for a wall temperature ratio of 0.2 or greater. Chien's tests were conducted at Mach 7.9. For a very cold wall temperature ratio of 0.11, the Spalding-Chi method is shown (fig. 13) to be best. However, shock tube experiments (refs. 61 and 62) at wall temperature ratios from 0.01 to 0.24 and at Mach numbers of 1.5 to 3.1 indicate the best agreement with Van Driest II in reference 61, while Ref. 62 supports using Spalding-Chi. In fact, reference 53 and Cary (ref. 63) concluded that the Spalding-Chi method yielded the best results over the entire temperature ratio range 0.1 to 0.7 at Mach numbers of 4 to 13. Charts of turbulent heat-transfer coefficients based on the Spalding-Chi correlations were made by Neal and Bertram.(ref. 64) Zoby and Graves (ref. 65) statistically studied the effect of using two different forms of Reynolds analogy on the Van Driest II, Spalding-Chi, and reference enthalpy methods. Data from ground-based facilities and from flight tests were analyzed. It was concluded the Colburn modification of Reynolds analogy, which is

$$St = \frac{c_f}{2Pr^{0.667}} \tag{52}$$

usually resulted in somewhat better agreement with test data than using von Karman's version of Reynolds analogy. A comparison of the three heat-transfer prediction methods with the data (ref. 65) typically yielded rms errors of 15% to 18%.

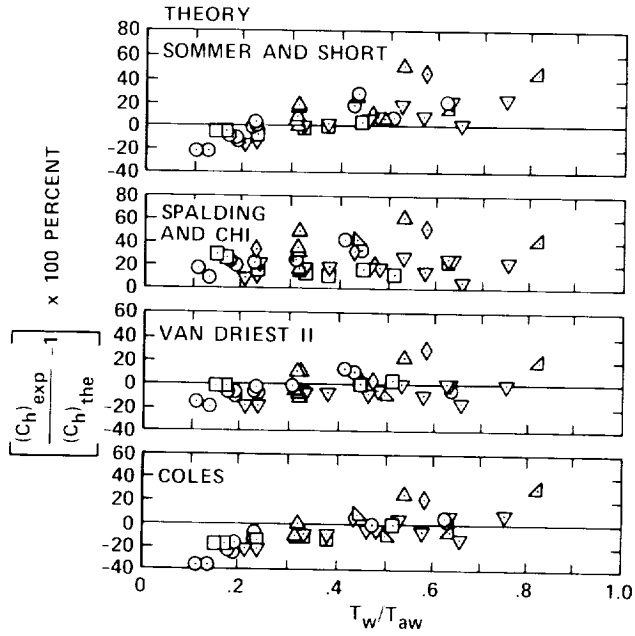

Figure 12.– Effect of wall-temperature ratio on predicted heat transfer. $M_e = 4.9$ to 7.4; $2C_h/C_f = 1.0$. (From ref. 52; reprinted with permission of The American Institute of Aeronautics and Astronautics.)

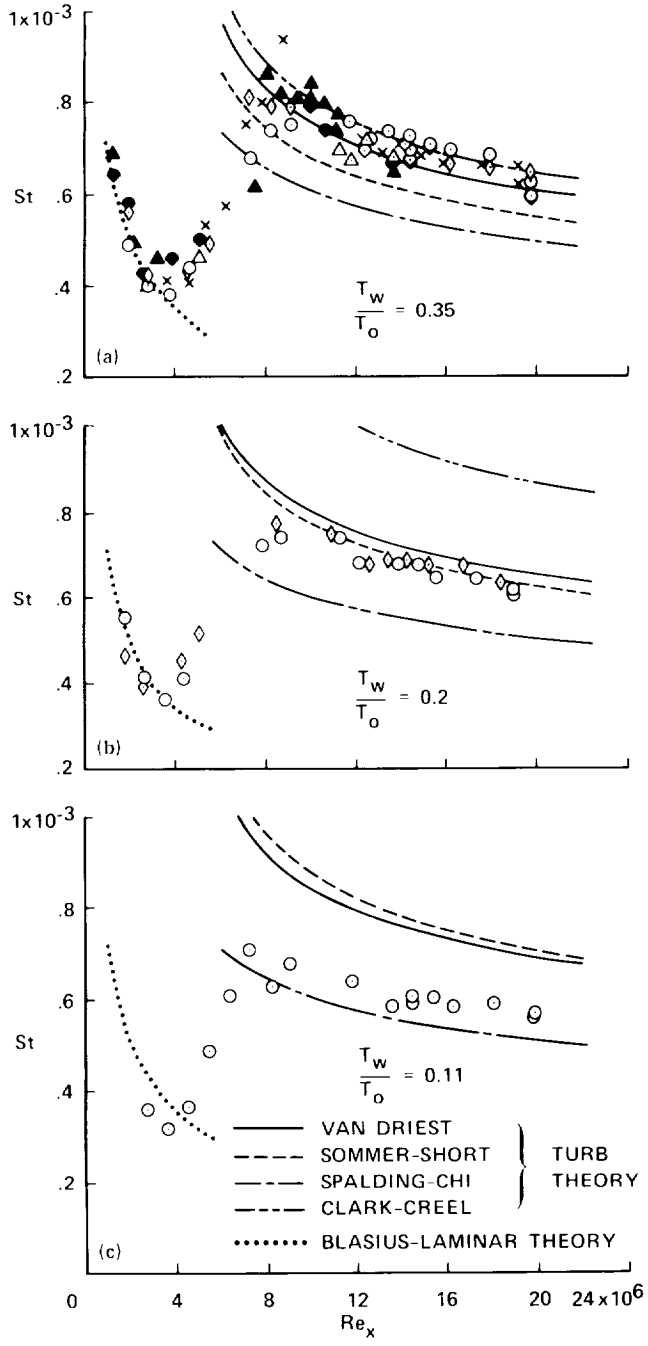

Figure 13.– Stanton number variation with Reynolds number and wall temperature ratio. (From ref. 60; reprinted with permission of The American Institute of Aeronautics and Astronautics.)

The conclusion is that all the semiempirical methods give only approximate results that can be off by 20%, or sometimes more. However, for wall temperature ratios below 0.2, Spalding-Chi does seem to predict the heating better than the other three methods. It should also be noted that finite-difference codes for calculating perfect gas turbulent boundary layer properties have been developed by Wilcox (refs. 66-68) and, no doubt, others.

4.2 Reference Enthalpy Method

The reference enthalpy method has been widely used for three decades. The most common expression for the reference value of the enthalpy (ref. 56) is

$$h' = 0.22h_{aw} + 0.28h_e + 0.5h_w \tag{53a}$$

although a number of variations have been used. At least one other version (ref. 8) given by

$$h' = 0.18h_{aw} + 0.32h_e + 0.5h_w \tag{53b}$$

yields slightly better results. The Eckert version, equation (53a), was used by Arthur et al. (ref. 69) to derive simple, closed-form correlation equations for the turbulent flat-plate heating. The Blasius incompressible, turbulent skin-friction relation was used in reference 69 for Reynolds numbers to 10 million in the form

$$\frac{c_f}{2} = \frac{0.0296}{(Re')^{0.2}} \tag{54}$$

and the Schultz-Grunow equation

$$\frac{c_f}{2} = \frac{0.185}{(\log_{10} Re')^{2.584}} \tag{55}$$

for Reynolds numbers above 10 million. In equations (54) and (55), the prime denotes that the quantity is evaluated at the conditions corresponding to the reference enthalpy. The thermodynamic and transport properties of references 5 and 6 were used to calculate the heat-transfer rate at altitudes from 3 to 60 km and at velocities from about 1 to 11 km/sec. The resulting correlation, which is valid to ±15% for $V_\infty > 1500$ m/sec, but less than 3960 m/sec

$$\dot{q}_{wFP} \approx \frac{3.72(10^{-4})(\rho_\infty \sin^2\delta \cos^{2.22}\delta)^{0.8}}{(x - x_{bl})^{0.2}(T_w/555)^{0.25}} \times V_\infty^{3.37}\left(0.9 - \frac{h_w}{H_e}\right) \quad \frac{W}{m^2} \tag{56a}$$

and for $V_\infty > 3960$ m/sec

$$\dot{q}_{wFP} \approx \frac{2.45(10^{-5})(\rho_\infty \sin^2\delta \cos^{2.62}\delta)^{0.8}}{(x - x_{bl})^{0.2}} \times V_\infty^{3.7}\left(0.9 - \frac{h_w}{H_e}\right) \quad \frac{W}{m^2} \tag{56b}$$

In equation (56) the Newtonian approximation for pressure and velocity were used in the form

$$p_e \approx \rho_\infty V_\infty^2 \sin^2\delta \tag{57}$$

$$u_e \approx V_\infty \cos \delta \tag{58}$$

Therefore, the heat transfer is underpredicted at small values of δ. (For example, at $\delta = 10°$, the heating will be about 6.5% too low, which is well within the uncertainty of the reference enthalpy method.) Note that for the beginning of the turbulent boundary layer, the location at which transition begins, x_{bt}, was chosen. While this choice is somewhat conservative, it is supported by the correlations of references 53 and 65. The turbulent heat transfer on a sharp cone of half angle, δ, would be given, approximately, by (ref. 8)

$$\dot{q}_{w_C} \approx 1.15\dot{q}_{w_{FP}} \tag{59}$$

The relations derived so far are valid if the boundary layer is either laminar or turbulent. In locating the effective origin of the turbulent boundary layer in equation (56), it was assumed that the transitional flow region is equal in length to the preceding laminar flow distance. For lack of a better model, it is assumed here that the heating rate in the transitional region varies linearly with distance, having the laminar value at the beginning of transition and the fully turbulent value at the end of transition. This approximation gives, roughly, the correct average skin friction according to Dhawan and Narasimha (ref. 70), and, therefore, the correct heating rate.

It is now possible to calculate the heat-transfer rate on a simple configuration. The example chosen here is the heating along the fuselage windward centerline of the Shuttle orbiter during the first flight (see fig. 14, from Tauber and Adelman (ref. 71)). The calculations were made using equations (48) and (56) by assuming that the bottom surface was a wedge at the local surface slope and in radiative equilibrium. The agreement between the measured values and the calculations is fairly good. The turbulent calculations are definitely too high, possibly because of the cold wall conditions or the conservative choice of the origin. The error bars on the data represent the effect of uncertainties in the surface emissivity (ref. 72). At the flight conditions shown in figure 14, molecular dissociation was sufficiently small to make catalytic wall effects unimportant in the laminar boundary layer. Finite-rate wall catalysis has not been observed in turbulent boundary layers, probably because of the intense mixing.

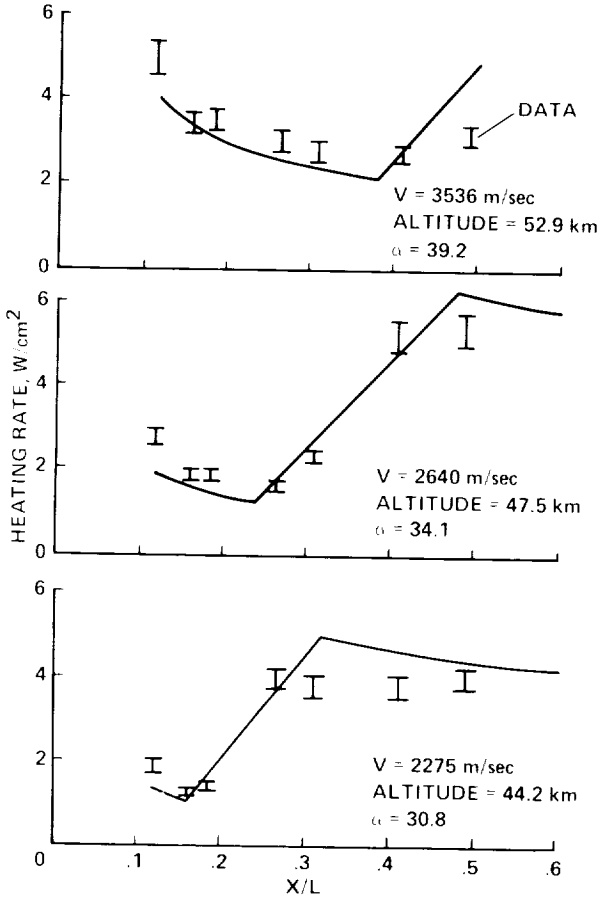

Figure 14.– Comparison of centerline heating calculations with STS-1 flight data. (From ref. 71.)

4.3 Cross-Flow and Surface Roughness Effects

Three-dimensional shapes, or axisymmetric bodies at angle of attack, all experience cross flows. The heating of such complex flows must, generally, be computed using finite-difference methods (refs. 73 and 74). However, for a few geometrically simple shapes, or in the plane of symmetry, approximate methods can be used. One such example is the calculation of the turbulent heating on the leading edge of a swept wing. The cross flow induced by the leading-edge sweep promotes boundary layer transition (ref. 51). Also, a turbulent boundary layer at the wing-fuselage junction can cause transition at the leading edge. To approximately account for the turbulent flow along the leading edge, equation (56) must be used for the flat-plate contribution in equation (49).

Another example where the heating in a complex flow can be treated approximately is the sharp cone at angle of attack. For this case, the tangent cone approximation (ref. 8) yields reasonably good results when the angle of attack is less than the cone half angle. In the tangent-cone method, an imaginary cone is used having a half angle which equals the slope of the local ray on the cone at angle of attack. However, when the cone also has a blunt nose, the heating distribution becomes more complex (see fig. 15, from Widhopf (ref. 75)) and must be calculated numerically (ref. 74).

Vehicles designed to fly at hypervelocities are usually protected by ablative heat shields. Frequently, ablation causes a rough surface which can trigger early boundary layer transition. Roughness-induced transition on blunt noses of bodies, where the boundary layer is thin and the flow subsonic, has been widely observed and studied (refs. 45-47). In addition to triggering premature transition, the surface roughness can increase the turbulent heating by over 100%. The turbulent heating caused by roughness elements equal in size to about 1% of the nose radius is illustrated in figure 16 (from Chen (ref. 76)). The peak rough-wall turbulent heating formulation of Chen predicts

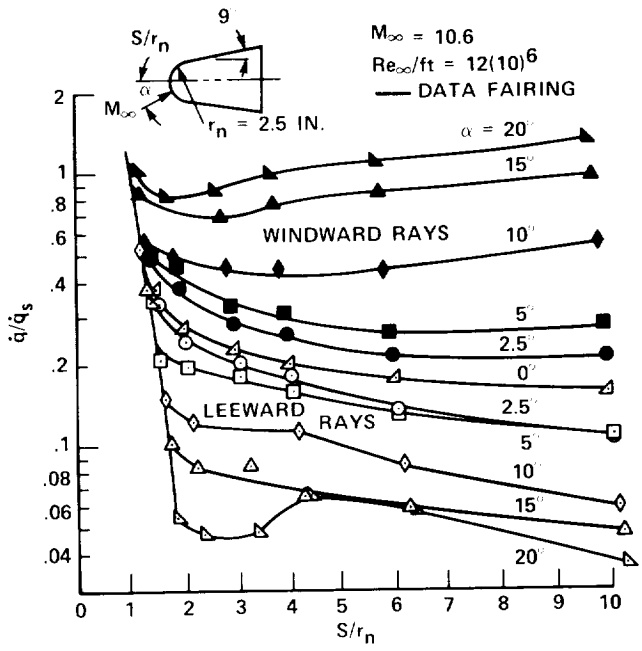

Figure 15.– Turbulent heat-transfer distributions along the windward and leeward rays for various angles of attack. (From ref. 75; reprinted with permission of The American Institute of Aeronautics and Astronautics.)

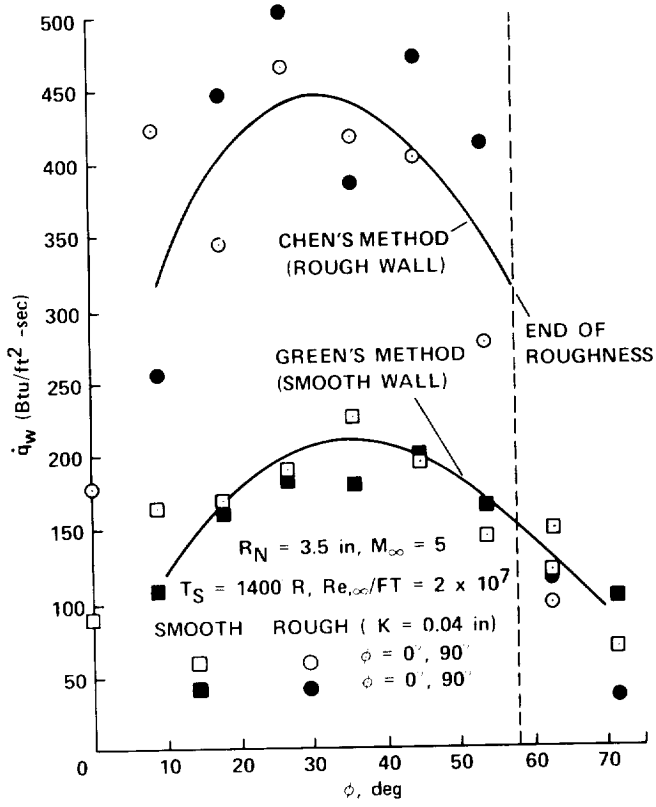

Figure 16.– Heat transfer to hemispheres having very rough and smooth walls in a typical tunnel environment. (From ref. 76; reprinted with permission of The American Institute of Aeronautics and Astronautics.)

more than twice the smooth-wall value and agrees reasonably well with the heavily scattered data. Note, also, that the peak heating rate occurs about 30° off the stagnation point, compared to 35° for the smooth surface value. The computation is performed by numerically integrating a set of modified turbulent boundary layer equations which are based on the assumption that the effect of roughness on the mixing is restricted to a relatively thin layer near the wall.

Next, the heating associated with regions of separated flow will be discussed. This will be followed by a brief coverage of shock-interaction heating.

5. SEPARATED FLOW AND SHOCK-INTERACTION HEATING

Although regions of separated flow occur frequently when control surfaces are deflected to large angles on hypersonic vehicles, the computation of such viscous flow fields is complex and relies heavily on finite-difference, numerical methods. Another mechanism that can cause flow separation, and severe local increases in heating near the flow reattachment point, is the presence of gaps, or cavities, and steps in the surface. The discussion of heating in cavities will be followed by a brief coverage of the heating experienced in the base regions of bodies. The extremely high local heating that can occur when shocks intersect is covered last.

5.1 Shock-Induced Separated-Flow Heating

In a supersonic or hypersonic flow, a shock is generated when the local surface slope increases abruptly. For example, such a change in slope occurs when a control surface is deflected. Since the static pressure increases through the shock, the higher pressure is fed upstream through the subsonic part of the boundary layer, which causes the flow to separate (fig. 17). For a given pressure increase, the extent of the separation region in a laminar boundary layer is greater than in a turbulent one since the former has a greater fraction of subsonic flow. A region of recirculating flow is formed in the corner with the fluid adjacent to the wall moving upstream. The heating in the separated-flow region is increased over the value ahead of the separated region and peaks at, or slightly beyond, where the boundary layer reattaches on the compression surface. The heating in separated and reattached flows has recently been reviewed by Merzkirch et al. (ref. 77).

Extensive heat-transfer measurements were performed by Holloway et al. (ref. 78) in laminar, transitional, and turbulent separated flows. The experiments were performed at Mach 6 and at maximum length Reynolds numbers from 0.9 million to 7.3 million. An example of the heat transfer in a turbulent boundary layer at Mach 6 with attached and separated flow on a 75° sweptback, sharp delta wing is

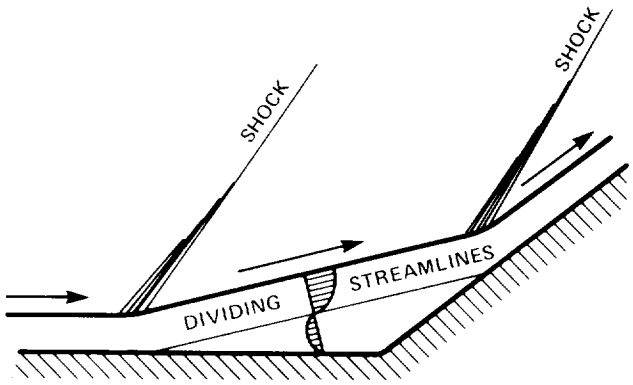

Figure 17.– Supersonic compression corner flow.

shown in figure 18 (from Keyes et al. (ref. 79)). The wing is at zero angle of attack. The flap deflection of 20° does not cause flow separation, whereas the deflection of 40° produces strong separation. (The problem of trying to calculate the heating on the flap is evident from the variety of methods used.) Various researchers have correlated the ratio of turbulent heating rates ahead of the separated region to the peak rates on the flap with the corresponding pressure ratio. Back and Cuffel (80) give the empirical relation

$$C_{h_2}/C_{h_1} = (p_2/p_1)^{0.85} \qquad (60)$$

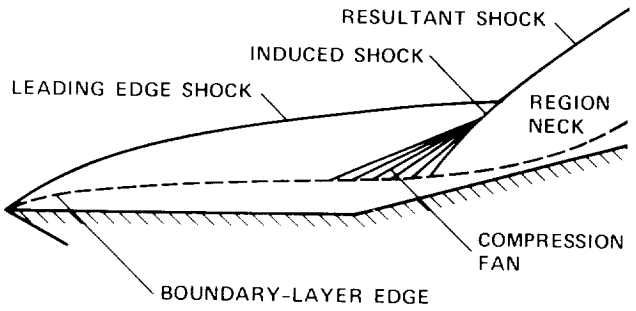

Figure 18.– Stanton number variation on 75° delta wing with trailing-edge flap. Re/m ≈ 2.7 x 10^7;α = 0°. (From ref. 79; reprinted with permission of The American Institute of Aeronautics and Astronautics.)

where their (dimensional) heat transfer coefficient is defined as

$$C_h = \dot{q}/(h_{aw} - h_w) \qquad (61)$$

Nestler (ref. 81) suggests an exponent of 0.80 in equation (60) and Alzner and Zakay (ref. 82) find values from 0.725 to 0.815 for turbulent flows.

For hypersonic laminar boundary layers, Mathews and Ginoux (ref. 83) suggest a relation in terms of Stanton number at peak heating, St_{max}, which is approximately

$$St_{max} \sim (Re_1)^{-0.5} \qquad (62)$$

where Re_1 is the Reynolds number ahead of the separated region on the flat plate. The constant of proportionality appears to be a strong function of wall temperature ratio.

The problem of determining the heating when flow separation occurs has been attacked successfully numerically. Shang and Hankey (ref. 84) calculated the supersonic flow field for the turbulent boundary layer case, while Hung and MacCormack (ref. 85) did the hypersonic, laminar case. More recently, Lawrence et al. (ref. 86) used a perfect gas parabolized Navier-Stokes (PNS) code to calculate the hypersonic flow on a sharp flat plate at zero angle of attack with a flap (fig. 19). (The flow field shown in fig. 19 could simulate the hypersonic flow over a sharp-nosed airfoil with a large flap.) A comparison of calculated laminar heat transfer with experimental data from reference 86 is shown in figure 20. At a Mach number of 14, the 15° deflection angle did not cause significant separation. A newer version of the code, incorporating real gas effects, was used to perform the same calculation as above, but at twice the previous Reynolds number and at a Mach number of 20 (ref. 87). The result is shown in figure 21. (Since the calculations were performed on different computers, no direct comparison of computation time is possible.) The heat-transfer coefficient of references 86 and 87 is defined as $C_h = Pr\ St(\rho_e u_e/\rho_\infty V_\infty)$.

Shock-induced boundary layer separation and increased local heating also occur when a shock wave impinges on the flow over a flat plate. Experiments performed by Back and Cuffel (ref. 88) in a turbulent boundary layer at Mach 3.5 confirmed the empirical relation given by equation (60), but gave an exponent of about 0.73. Skebe et al. (ref. 89) performed detailed boundary layer measurements of the effects of shock interactions on a flat plate having initial laminar, transitional, and turbulent flow. The Mach numbers ranged from 2 to 4 and Reynolds numbers per meter varied from about 4.7 million to 30 million.

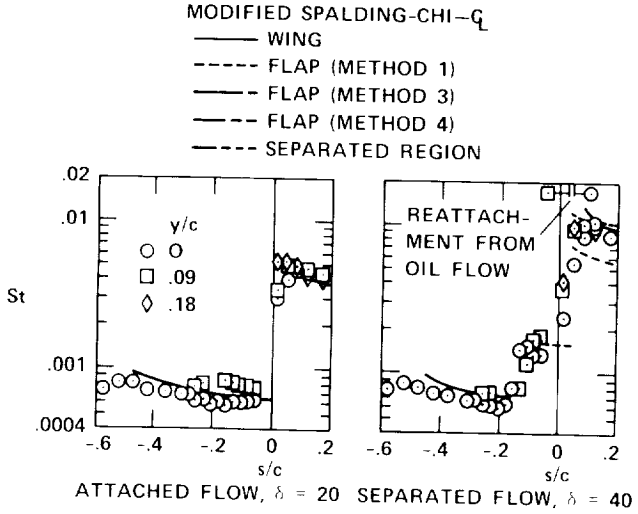

Figure 19.– Hypersonic compression corner flow

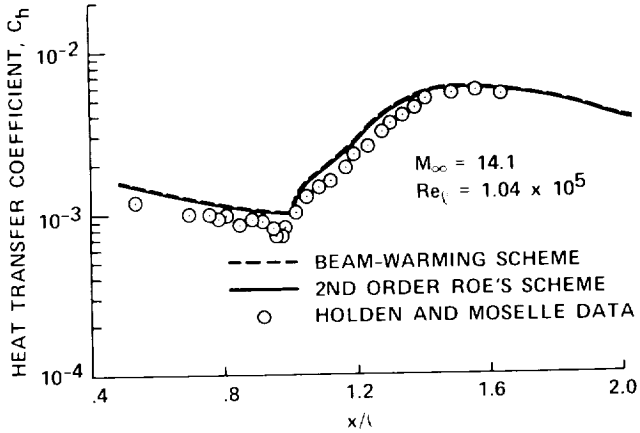

Figure 20.– Comparison of heat-transfer coefficients on sharp flat plate with 15° compression corner. (From ref. 80; reprinted with permission of The American Institute of Aeronautics and Astronautics.)

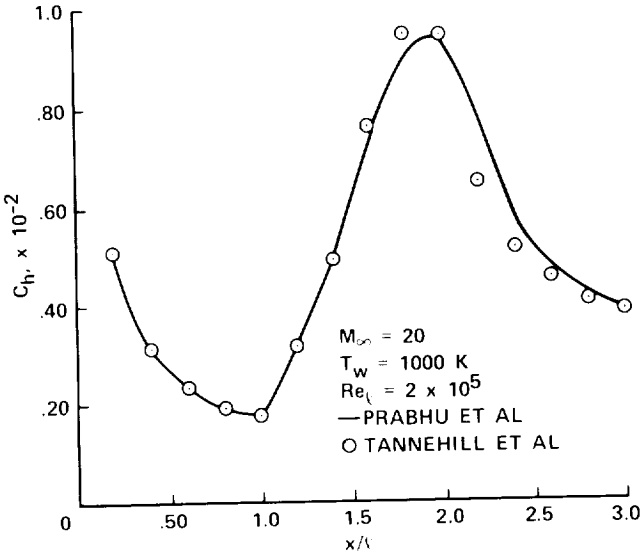

Figure 21.– Comparison of heat-transfer coefficients on sharp flat plate with 15° compression corner. (From ref. 87; reprinted with permission of The American Institute of Aeronautics and Astronautics.)

Detailed boundary layer surveys were made, but heat transfer was not measured. Hodge (ref. 90) compared numerical calculations using MacCormack's code (ref. 85) with pressures measured for laminar boundary layer shock interactions at Mach 8. He found good agreement except near the beginning of the induced separation region. Hung et al. (ref. 91) present correlations for the peak heating from shock impingement on a flat plate at hypersonic speeds. The following expressions for the Stanton numbers at peak heating are given in reference 91:

for laminar/laminar flow

$$St_{max} \approx 0.664(Re'_x)^{-0.5}(Pr')^{-0.667} \qquad (63)$$

for laminar/turbulent and turbulent/turbulent flow

$$St_{max} \approx 0.0576(Re'_x)^{-0.2}(Pr')^{-0.667} \qquad (64)$$

where the prime denotes that the parameter is based on the reference enthalpy value (eq. 53a) at the peak heating location. Viegas and Coakley (ref. 92) studied turbulence models that were used in the Navier-Stokes equations to calculate shock-separated turbulent boundary layers. They concluded that the one-equation model proposed by Glushko and Rubesin gave superior results, including more accurate skin-friction values, than the zero equation model.

5.2 Heating in Cavities

Cavities occur on all vehicles and can cause large increases in local heating at high speeds. First, cavities can trigger boundary layer transition. Second, the heating within the cavity can be much higher than the heating of the surface just ahead of the cavity. Experiments of heating within cavities in turbulent flows were reported by Nestler et al. (ref. 93) and some of their results are shown in figure 22. The ratio of the flat-plate heating rate to that measured within the cavity is shown in figure 22; C_h is defined by equation (61). (The curves have been drawn through the original data points, which are deleted.) The Mach number on the plate was 6.3 and the local Reynolds number was about 6 million. The turbulent boundary layer thickness just ahead of the cavity location was 1 cm. For the cavity length-to-depth ratio (L/H) used in figure 22 of 5, 15, 30, the cavity depth was 2.5 cm, 2 cm, and 1 cm, respectively. Note that for L/H = 5, the flow passes over the cavity and the heating on the cavity floor is decreased from the undisturbed flat-plate value. When L/H ≈ 11, the nature of the flow in the cavity changes according to Gortyshov et al. (ref. 94). For values of L/H larger than 11, the flow expands into the cavity, attaches on the floor, and separates near the downstream corner, where the heating near reattachment reaches three times the undisturbed flat-plate value.

For supersonic turbulent flow, the average heat transfer in the cavity is (ref. 94)

$$St_{ave} = 0.48(Re_L)^{-0.4}(L/H)^{0.2} \qquad (65)$$

where the Stanton and Reynolds number properties are evaluated using the undisturbed flow conditions and the cavity length (ref. 77). For cavities in supersonic and hypersonic laminar boundary layers, Lamb (ref. 95) gives the following expression:

$$St \approx 2.07(Re_\delta)^{-1} \qquad (66)$$

In equation (66), the Reynolds number is, again, evaluated at the flow conditions upstream of separation and is based on the boundary layer thickness, δ, ahead of the cavity, while the Stanton number is related to the heating on the leeward surface (ref. 77).

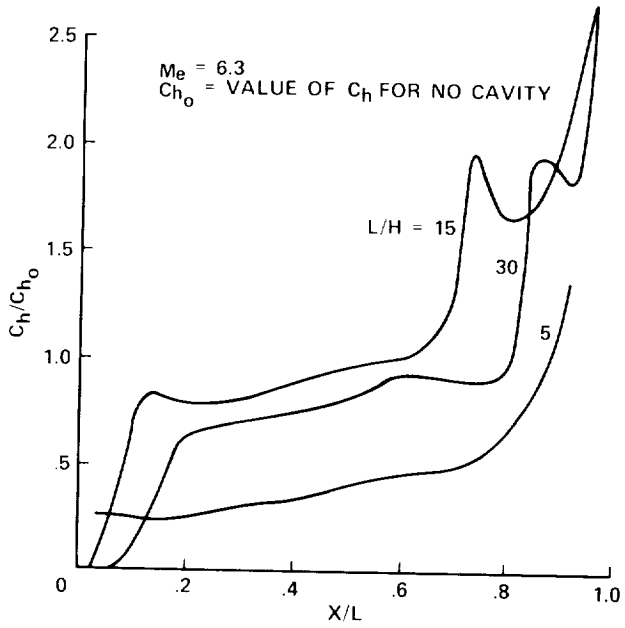

Figure 22.– Relative heat-transfer coefficient measured along cavity floor. (From ref. 93; reprinted with permission of The American Institute of Aeronautics and Astronautics.)

5.3 Heating in Base Regions

Since the heating in the base regions of hypersonic vehicles is one to two orders of magnitude less than on the windward portions of most vehicles, the topic will be discussed only briefly. Francis (ref. 96) presents flight data for ablating very slender (4.5° half-angle) cones with turbulent boundary layers. For a blunted cone, the heating in the base region was, approximately, 6% of the cold wall value without ablation on the cone afterbody. Bulmer (refs. 97 and 98) gives a correlation for turbulent flow base heating on cones in hypersonic flow in the form

$$\frac{(Nu/Pr)_b}{(Nu/Pr)_c} = 35.5(Re_b/Re_c)^{2.2} \qquad (67)$$

In equation (67), the subscript b refers to the evaluation at conditions where the flow has expanded isentropically to the base pressure and the reference length is the base radius. The subscript c refers to the flow conditions on the cone just ahead of the base (ref. 77). For base heating where a laminar boundary layer exists, reference 77 suggests using equation (66).

5.4 Shock-Interference Heating

Shock-interference flows occur when, for example, the bow shock from the blunt nose of a vehicle impinges on the leading edges of wings, fins, and inlet cowl lips. The analysis of shock-interference heating is fundamentally complex, but cannot be ignored because heating rate increases of one order of magnitude have been observed. The intersection of strong shock waves can produce free shear layers, jets, or expansions. Different shock interactions and the resultant flows were delineated and studied by Edney (ref. 99). In reference 99 it was found that large increases in heating result from free shear layer attachment and supersonic jet impingement. Keyes and Morris (ref. 100) performed experiments at a free-stream Mach number of 6. Turbulent shear layer attachment on a hemisphere was found to produce local heating rates which were up to 14 times higher than the undisturbed stagnation point value. An approximate correlation for the ratio of peak local heat transfer to the (undisturbed) stagnation point value (ref. 100) can, again, be written using the corresponding pressure ratio, in the form

$$Ch_p/Ch_s \approx C(p_p/p_s)^{1.35} \qquad (68)$$

where C = 1.58 when the shear layer is turbulent and C = 0.63 when it is laminar. The dependence of the heating on the shear layer state (laminar, turbulent, or transitional) is, again, emphasized by Keyes (ref. 101). It is shown that the initial state of the shear layer can have a major influence on the heating.

6. HEAT-PROTECTION METHODS

The preceding discussion has been limited to methods of calculating the heating rates at the body's wall in the absence of interactions with the surface, i.e., the cold wall heating. The following discussion will deal with methods of protecting the body surface from the aerodynamic heating.

Several heat-protection methods are widely used. If the heating rate and duration of the pulse is modest, a high-heat capacity metal heat sink, such as Beryllium oxide, can absorb about 6.3 MJ/kg (about 2700 Btu/lb). For many purposes, a more effective mechanism of heat absorption is to transfer mass from the surface to the boundary layer. The three main methods of mass-addition cooling are described below.

Film cooling: fluid is injected into the boundary layer near the stagnation point, from where it spreads back over the body.

Transpiration cooling: the fluid passes through a porous wall into the boundary layer. This differs from film cooling in that fluid injection can occur all along the wall.

Ablation: the surface material is allowed to melt and vaporize, and enters the boundary layer in a liquid or gaseous state. The mass addition of fluid into the boundary layer reduces heat transfer by (1) absorbing heat through phase changes of the material from solid to liquid to gas and (2) thickening the boundary layer and altering the velocity profile. Ablative heat shields are frequently impregnated with carbon fibers. The fibers provide structural reinforcement and, at high temperatures, form a char layer. The char is porous and permits percolation of gases and reradiates

heat. For example, at a temperature of 3000 K, over 400 W/cm^2 can be reradiated.

To protect the structure and the interior components of the vehicle, insulation material is required between the heat shield and the structure. Since the heat transfer occurs by conduction, materials having low conductivity and low density are used.

6.1 Mass-Addition Cooling

The most widely used method of protecting vehicles against the high heating encountered in hypervelocity flight is mass-addition cooling. An early study of (stagnation region) film cooling was made by Howe and Mersman (ref. 102). Low (ref. 103) calculated the effect of transpiration cooling on the laminar boundary layer on a flat plate in supersonic flow where the injectant was air. Subsequently, Pappas and Okuno (refs. 104-106) measured the influence of injecting various gases, which were both lighter and heavier than air, on the heat transfer on cones, having laminar and turbulent boundary layers, in supersonic flow. Kaattari (ref. 107) and others performed mass-injection experiments on blunt-nosed bodies, including hemispheres. The results of the fluid-injection experiments were correlated for laminar boundary layers in reference 23. For the turbulent case, the coefficients were found empirically. The correlation is, using an expression of the form (ref. 7)

$$\psi = \dot{q}_w/\dot{q}_{wB=0} = 1 - a(\bar{m}_e/\bar{m}_w)^n B + b(\bar{m}_e/\bar{m}_w)^{2n} B^2 \quad (69)$$

where $\bar{m}_e$ and $\bar{m}_w$ are the molecular weights of the shock-layer gas and the injection gas, respectively. The dimensionless mass-addition parameter, B, is defined as

$$B = \frac{\dot{m}_w}{\dot{q}_{wB=0}}(H_e - h_w) \quad (70)$$

where $\dot{m}_w$ is the mass-addition rate. The constants a, b, and n in equation (69) have the following values:

	a	b	n
Stagnation point (lam.)	0.72	0.13	0.25
Cone, or flat plate (lam.)	0.795	0.11	0.25
Cone, or flat plate (turb.)	0.29	0.015	0.5

The results from equation (69) are compared with the measurements of references 104-107 by plotting the heating reduction as a function of the mass-addition parameter. In figure 23, the heating reduction is shown when air is injected into an air boundary layer, $\bar{m}_w = \bar{m}_e$, at the stagnation point and on cones, or flat plates, having laminar and turbulent flow. The agreement is good. It is also apparent that a much higher injection rate is required to cool the wall when turbulent flow exists, as confirmed by Dershin et al. (ref. 108). The effect of molecular weight ratio on the agreement between equation (69) and the data is illustrated in figure 24 for laminar flow. Again, the agreement is reasonably good. The beneficial effect of injecting gases which are lighter than air is evident. Since lighter gases thicken the boundary more than heavy ones, the velocity gradient in the boundary layer is reduced more. (For Freon, $\bar{m}_w \approx 120$ was used.) The influence of molecular weight ratio is more pronounced for the turbulent boundary layer than for the laminar one, as is evident in figure 25. For gases that are heavier than air, equation (69) underpredicts the wall cooling. Note also in figure 25 that in the turbulent flow case, the mass-injection efficiency decreases with increasing edge Mach number. This observation is confirmed by Jeromin (ref. 109) in his lengthy

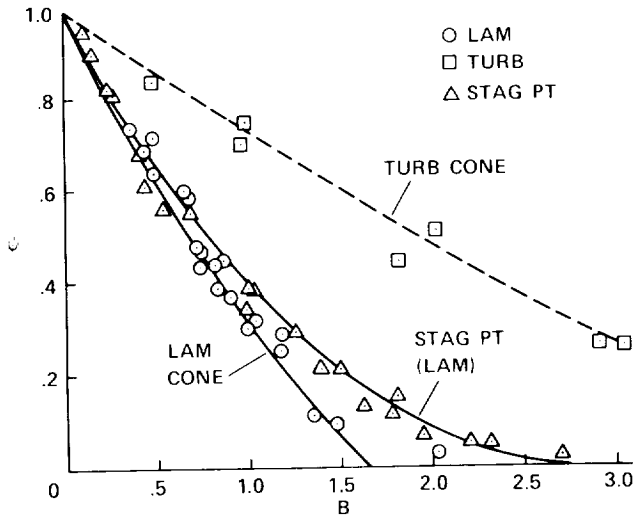

Figure 23.– Heat-transfer decrease at supersonic speeds for injection of air into air. (Laminar theory from ref. 23; data from refs. 104-107.)

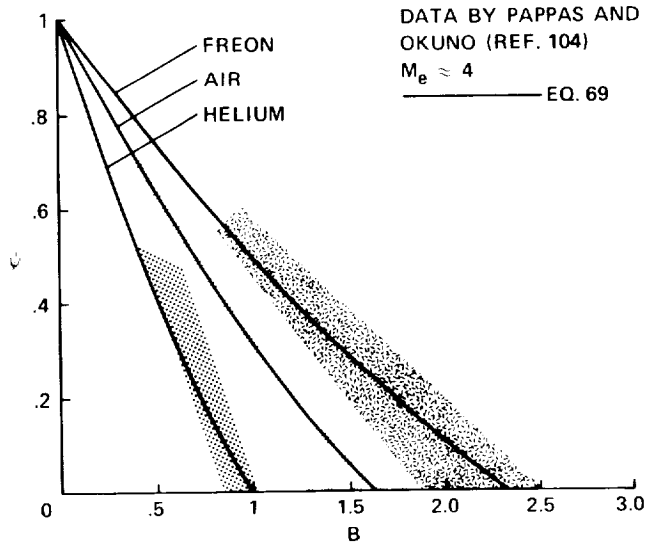

Figure 24.– Laminar heat-transfer decrease at supersonic speeds on sharp cone for three injected gases. (Theory from ref. 23; data from ref. 104.)

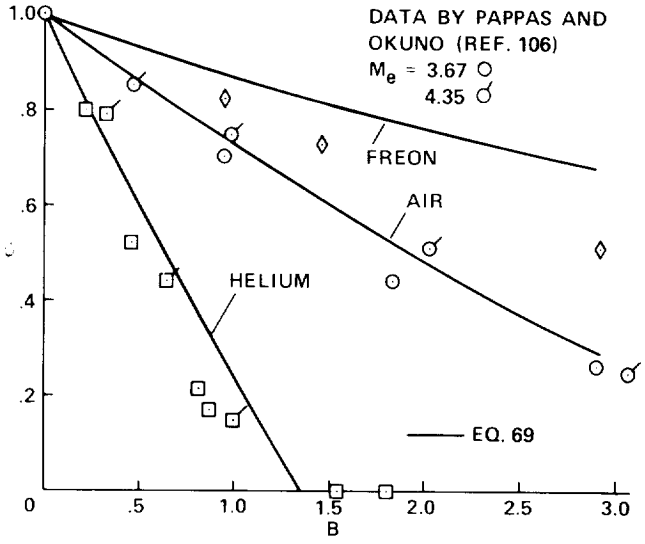

Figure 25.– Turbulent heat-transfer decrease at supersonic speeds on sharp cone for three injected gases. (Data from ref. 106.)

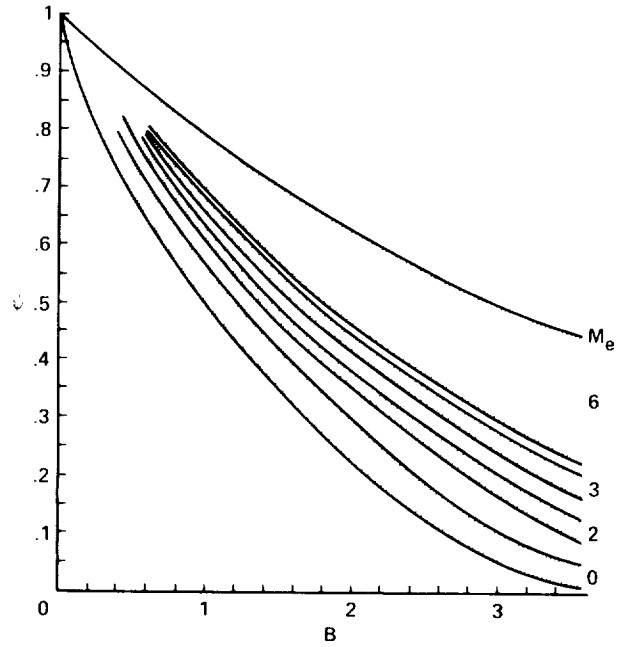

Figure 26.– Reduction of Stanton number for air injection (experimental data) on flat plates and cones with turbulent boundary layers. (From ref. 109.)

survey paper and is shown more dramatically in figure 26 (based on ref. 109).

Expressions such as equation (69) can be used to approximate the behavior of relatively low-temperature vaporizing ablators, for example, Teflon. For high-temperature, carbonaceous ablators, the presence of chemical reactions between the injected and resident species in the boundary layer must be included in addition to the surface radiation. Neither of these phenomena is accounted for in equation (69). The performance of carbon ablators was calculated by Putz and Bartlett (ref. 110), who derived empirical relations, similar to equation (69), for several materials. A stagnation point correlation for graphite, from numerical solutions, is (ref. 110)

$$\psi' = 1 - aB + bB^2 + cB^3 - dB^4 \qquad (71)$$

where $a = 0.6563$, $b = 0.01794$, $c = 0.06365$, and $d = 0.01125$. The previously defined heat-transfer ratio, ψ, is related to equation (71) by

$$\psi = \psi' + \left(\frac{\Delta H_c}{H_e}\right) \Big/ \left(1 - \frac{h_w}{H_e}\right) \qquad (72)$$

where the enthalpy ratio $\Delta H_c/H_e$ accounts for gas-phase chemical reactions and diffusion effects for injected species. The variation of ψ with the mass-addition parameter, equation (71), is shown in figure 27 and the enthalpy ratio from chemical reactions is given in figure 28. (Both figures are from ref. 110.)

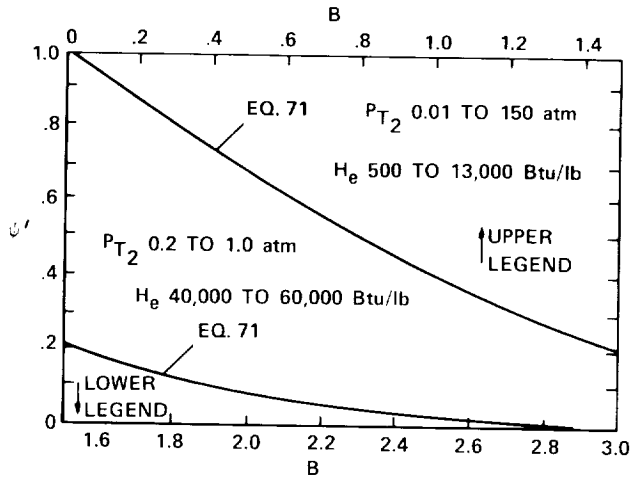

Figure 27.– Correlation of blowing parameter with graphite ablation boundary layer solutions. (From ref. 110; reprinted with permission of The American Institute of Aeronautics and Astronautics.)

Slender vehicles can experience very high heating at the nose in hypervelocity flight, causing surface recession and shape change at the nose. If the nose ablation is asymmetric, an undesirable pitching moment results. The slender-vehicle nose-ablation problem is formulated and the results of numerical solutions are presented by Chin (ref. 111). The roughness of the ablating surface can also cause premature boundary layer transition, which further intensifies the heating, as previously mentioned. The effects of nose surface roughness on transition and heating are discussed by Grabow and White (ref. 112). Slender-body nose-shape changes as determined from wind tunnel tests using low-temperature

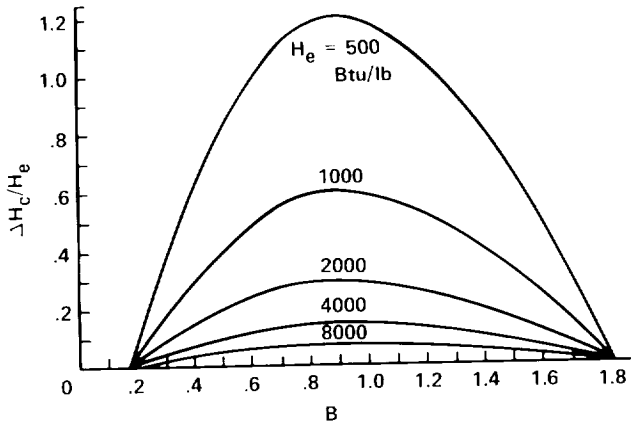

Figure 28.– Variation of $\Delta H_c/H_c$ with blowing rate and total enthalpy. (From ref. 110; reprinted with permission of The American Institute of Aeronautics and Astronautics.)

ablators were measured by Kobayashi and Saperstein (ref. 113). Using film cooling to reduce the surface recession and shape change of slender noses was studied by Gold et al. (ref. 114). The heat protection by mass injection was also theoretically studied for other geometric shapes and will be briefly covered next.

The effect of mass injection on the laminar heating along the stagnation line of an infinite, swept cylinder was calculated by Libby and Kassoy (ref. 115). For massive blowing, it was found that the spanwise flow separated, but the chordwise flow remained attached. Wortman analyzed the effect of mass addition on several blunt shapes ranging from hemispheres to cylinders (refs. 116 and 117). In references 116 and 117 the laminar boundary layer equations are solved for a real gas in equilibrium and for a variety of light and heavy (compared to air) injected gases. The results are presented in the form of correlation functions. In reference 118, Wortman calculates the reduction of laminar heating by mass injection on sharp cones at angle of attack. It was found that normalizing the heat transfer by the zero angle of attack values eliminated the influence of injected gas properties. Inger and Gaitatzes (ref. 119) computed the effect of strong blowing on high Reynolds number laminar flow, at supersonic speeds, about slender bodies, including induced pressure effects. Some of the effects computed in references 118 and 119 are open to question, however. For example, it is well known that cross flow on cones at large angles of attack (ref. 118) can induce boundary layer transition. It has also been observed that massive blowing at high Reynolds numbers can cause transition very close to the stagnation point of a blunt body, as will be discussed next.

6.2 Injection-Induced Transition

Demetriades et al. (ref. 120) and Kaattari (ref. 107) observed boundary layer transition caused by mass injection on blunt bodies in hypersonic flows. The effect was observed at Reynolds numbers based on body diameter as low as about 1 million. Similar results were observed by Wimberly et al. (ref. 121) on a slender cone tested at a free-stream Mach number of 12.2 and a free-stream Reynolds number of 4 million. In most of the cases observed, the occurrence of transition raised the heating above the laminar value without mass addition. Park (ref. 122) presented calculations to explain the injection-induced early transition on blunt bodies. However, no general method is available for predicting the injection rates that will lead to premature transition.

6.3 Ablation Material Response

To calculate the response of an ablation material to high heating rates, it is necessary to know the high-temperature properties of the material. Eighty-five different graphitic materials were tested by Lundell and Dickey (refs. 123 and 124). The pressures ranged up to 4.5 atm and temperatures up to 4000 K. The materials that were studied included ATJ graphite, both two- and three-dimensional carbon-carbon composites, pyrolytic graphite, mesophase graphite, glassy carbon, and natural graphite. It was found that ATJ graphite performed slightly better than the single-phase materials (pyrolytic graphite, mesophase graphite, and glassy carbon). However, at temperatures above 3600 K the ATJ mass loss increased exponentially with temperature. The mechanism responsible for the greatly increased mass loss was particulate removal, or spallation, probably caused by compressive thermal stress.

A different class of ablation materials consisting of ceramics was studied by Ziering (ref. 125). Metallic and ceramic materials have much greater mechanical strength than graphite, for example, and would experience much less erosion when traversing dust or rain clouds. Tests of the following materials were reported in reference 125: silicon nitride, silicon carbide, tantalum carbide, and tungsten. Silicon nitride's mass loss, surface recession, and energy absorbed per unit mass were found to be by far the best of the group, with silicon carbide rating a distant second. The energy absorbed per unit mass ablated was 6 MJ/kg (2600 Btu/lb) for silicon nitride, while silicon carbide's value was 0.72 MJ/kg (310 Btu/lb).

For additional information on the application of mass-transfer cooling, Hartnett (ref. 126) is recommended.

7. FINITE-DIFFERENCE CODES

A large number of computer codes exist which can be used to calculate heat transfer at high velocities. Most of these codes were not intended for widespread use and have never been documented. By necessity the following discussion will be limited to a small, but representative, sampling of codes that are being used to calculate cold-wall aerodynamic heating. The discussion concludes with a description of some codes that can be used to compute surface ablation.

Thompson et al. (ref. 127) compared the heating on blunted slender cones at angles of attack as calculated by

four different codes with both wind tunnel and flight data. The codes consisted of a three-dimensional, viscous flow, finite-difference method called VSL3D, and three approximate, engineering-type codes known as MINIVER, AEROHEAT, and INCHES. As expected, VSL3D gave the best agreement with the data. Of the approximate methods, MINIVER predicted the nose bluntness effects poorly and AEROHEAT underpredicted the laminar flow heating at angle of attack by as much as 30%. The INCHES code gave good results at zero angle of attack, but at small angles of attack the windward ray heating was underpredicted by up to 40%. However, the engineering-type codes all used small amounts of computer time and their utility must be evaluated in that light.

7.1 Space-Marching Codes—PNS

The most widely used methods to calculate hypersonic flow fields and heat transfer are the downstream marching solutions of the parabolized Navier-Stokes equations known as PNS codes. The parabolized approximation is valid if the steady-state shock-layer flow, which must be supersonic, and the subsonic portion of the viscous-layer flow are both in the streamwise direction. Therefore, flows with large amounts of separation, and the attendant reverse flow, cannot be treated; however, cross-flow separation is permitted. When the above limitations are imposed, the Navier-Stokes equations becomes parabolic in the streamwise direction, thus permitting the downstream marching from an initial, supersonic data plane. Chaussee (ref. 128) evaluated the ability of a perfect gas PNS code to predict heat transfer on a blunted bicone having laminar and turbulent boundary layers. Comparisons with Mach 8 wind tunnel data gave reasonably good results when the damping coefficients (artificial viscosity) were held at the smallest value giving stable solutions. Chaussee and Rizk (ref. 129) used the same PNS code to make calculations of the flow over deflected control surfaces on several body shapes. The flap deflections were kept small enough to avoid separating the turbulent boundary layer. Although heating rates were not calculated, pressure distributions and other flow-field information were presented. Rizk et al. (ref. 130) used the PNS code to calculate heating on a bicone at angle of attack on the windward, leeward, and 90° plane. Their results were compared with wind tunnel measurements made at Mach 10 and are shown in figure 29 (from ref. 130). The comparison shows some disagreement near the nose of the vehicle. The differences on the aft part of the lee side are due to boundary layer transition which the code cannot predict.

The PNS code calculations of references 128-130 were made assuming a perfect gas. It would be surprising if the aerodynamic heating in a Mach 10 flow could be accurately predicted using the perfect gas assumption. In fact, Balakrishnan and Chaussee (ref. 131) showed that using

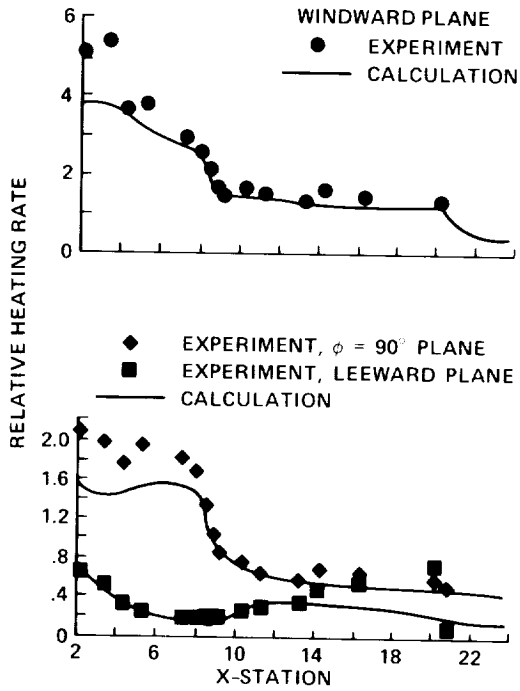

Figure 29.– Axial variation of the heat-transfer rate. $Re_d = 8.3 \times 10^4$; $\alpha = 10°$. (From ref. 130.)

perfect gas calculations caused the stagnation point heating to be significantly underpredicted at high speeds. Efforts to explain Shuttle orbiter surface-temperature measurements provided one impetus to include real gas effects in PNS codes. Prabhu performed this task and added the capability to compute chemical nonequilibrium effects (refs. 132 and 133). Subsequently, Prabhu et al. (ref. 134) extended the PNS code to permit three-dimensional flow computations. Examples of Prabhu's calculations are shown in figure 30, for a real gas in chemical equilibrium, and in figure 31 for the chemically reacting flow. Both figures 30 and 31 are for sharp cones having a 10° half angle, flying at a speed of 8100 m/sec at an altitude of 61 km. The small cone angle results in an equilibrium shock layer temperature of 3100 K at zero angle of attack. The relatively low temperature limits the nonequilibrium effects. Tannehill et al. (ref. 135) modified a PNS code (ref. 86) to include chemical reactions and also added an upwind-differencing algorithm. The upwind-differencing method improves shock capturing and avoids the instabilities inherent in central-differencing schemes caused by flow-field discontinuities such as shocks. The amount of artificial viscosity that is needed to control the oscillations occurring in central-differencing schemes can lead to inaccuracies in the computed results, as was observed in reference 128.

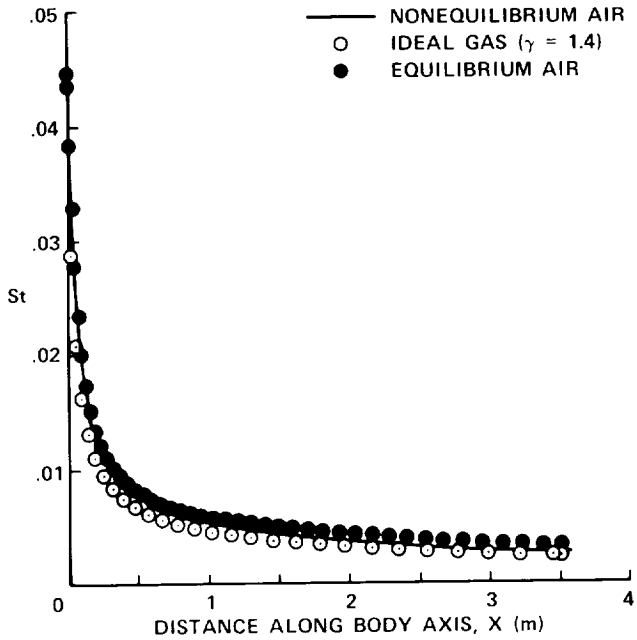

Figure 30.– Axial variation of Stanton number on 10° sharp cone for various gas models, $\alpha = 0$. (From ref. 132.)

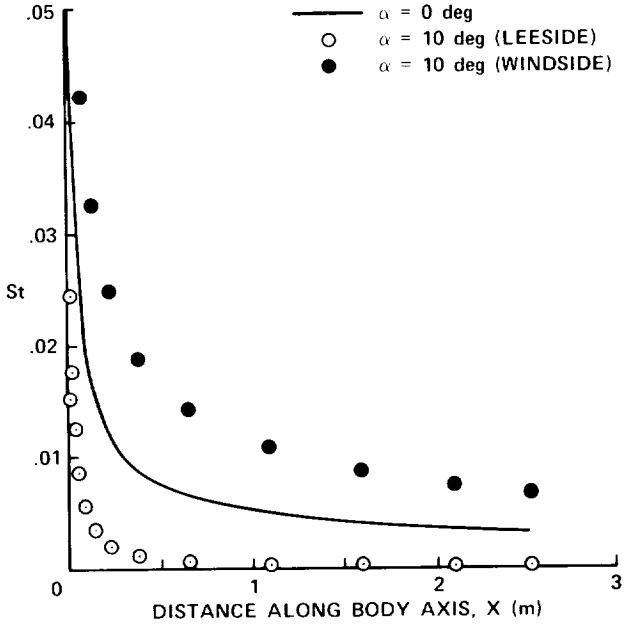

Figure 31.– Effect of angle of attack on 10° sharp cone heat transfer. (From ref. 134; reprinted with permission of The American Institute of Aeronautics and Astronautics.)

7.2 Time-Iterative Codes

To overcome the inherent limitations of the PNS codes, new methods are being developed to calculate the hypervelocity, real gas flow about three-dimensional bodies. The new codes use a time-iterative procedure which eliminates the need for artificial viscosity. However, the computation time for the time-dependent methods is nearly two orders of magnitude greater than for the downstream marching codes.

One example of a recently developed time-iterative code is the work of Palmer (ref. 136). Palmer's code employs an implicit, flux-splitting, shock-capturing method and includes equilibrium, real-gas effects. The code is being extended to treat chemical reactions (ref. 137).

Edwards et al. (ref. 138) compared four computer codes by using each to calculate hypersonic flow over two different bodies. The four codes consisted of an upwind PNS solver, UPS (ref. 86), and three time-iterative methods which solved the three-dimensional, thin-layer Navier-Stokes equations. The time-iterative codes consisted of a central-differencing, time-variational, diminishing code known as VAIR3D/TVD, a partial flux-split code called F3D, and an upwind solver, UWIN. A comparison of wind tunnel measured heating rates with calculations using the above codes is shown in figure 32 (from ref. 138). The comparison is for a bicone model at Mach 10 and a 10° angle of attack. All the codes give similar results with minor exceptions. Near the body's nose, the heating in the 90° meridional plane is underpredicted. Also, the occurrence of boundary layer transition on the leeward side increases the measured heating well above the calculated laminar flow values. (None of the codes can predict transition.) A second comparison of the codes with each other is illustrated in figure 33. A generic, hypersonic body shape was used; the body is to be tested in the NASA Ames 3.5-ft hypersonic wind tunnel. Note that the heat-transfer coefficients, computed at Mach 7.4 and $\alpha = 10°$, vary by over a factor of 2. Apparently the strong cross flow occurring on the body at angle of attack poses difficulties for all four codes, although about 70,000 grid points were used. Unfortunately, no experimental data are available yet to determine which of the four codes gives the best results under these conditions. The CPU time for the three time-iterative codes ranged from 37 to 90 min on the CRAY X-MP, compared to about 1 min for the UPS, space-marching code. Although great strides have been made using finite-difference methods to compute the (cold-wall) heat transfer on three-dimensional bodies, complex viscous flow fields still pose difficulties.

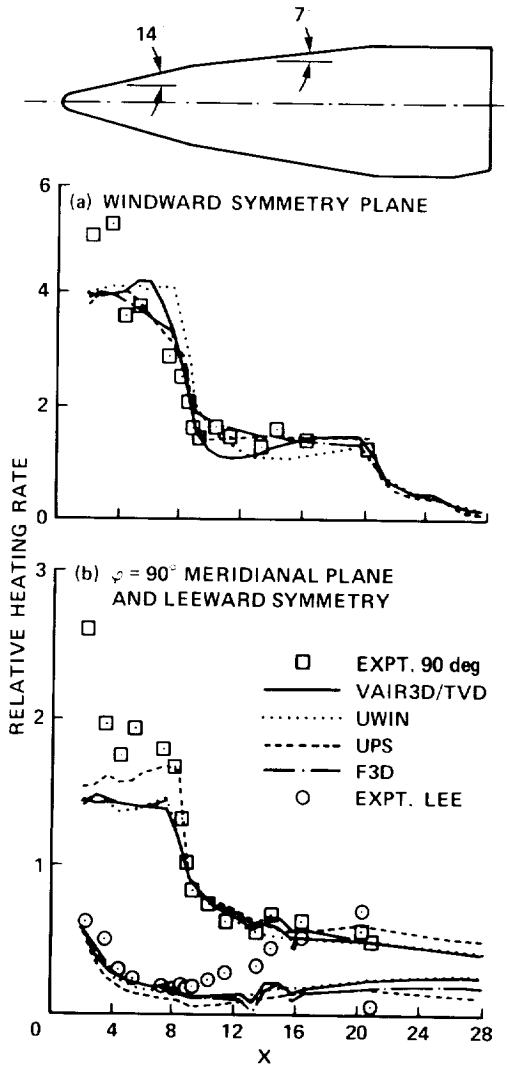

Figure 32.– Comparisons of heat-transfer rate for bicone. $M_\infty = 10$, $\alpha = 10°$. (From ref. 138.)

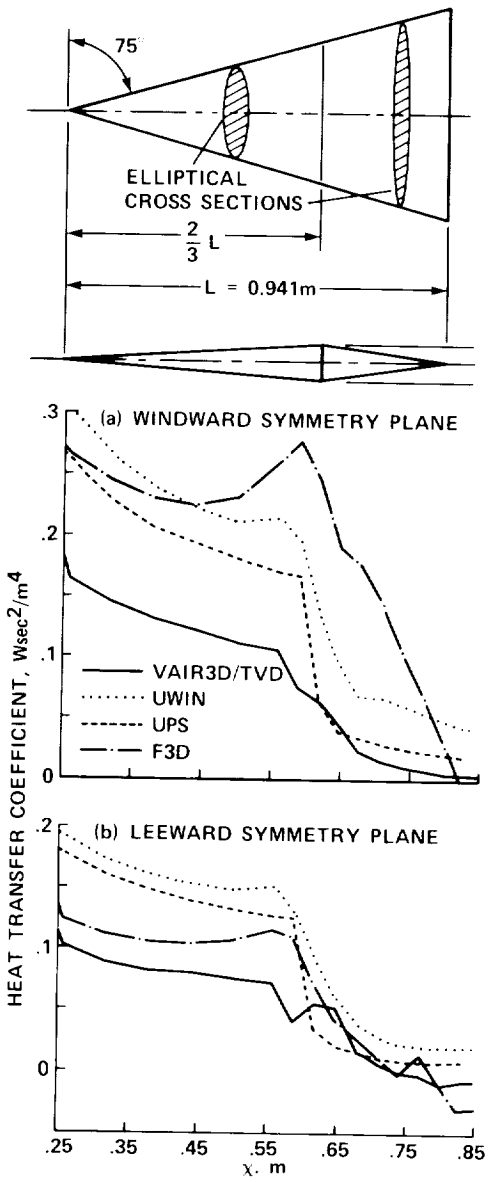

Figure 33.– Comparison of heat-transfer coefficients. $M_\infty = 7.4$, $\alpha = 10°$. (From ref. 138.)

7.3 Ablation Material Interaction Codes

Compared to the calculation of cold-wall heating, the interaction between the boundary layer and an ablating surface can be much more complex. Several codes which can be used to calculate mass-addition effects with chemical reactions will be discussed. The codes can be used to calculate ablative heat-shielding requirements.

The boundary layer integral matrix procedure (BLIMP) code (ref. 139) was developed to calculate the effects of chemical nonequilibrium in laminar and turbulent boundary layers over surfaces of arbitrary catalycities. The procedure is applicable to nonsimilar, multicomponent, laminar boundary layers with thermal diffusion and second-order, transverse curvature effects. The surface boundary conditions include coupling with transient ablation energy and mass balances. The BLIMP code has been used to analyze the surface catalytic effects experienced on the Shuttle orbiter (ref. 10). A relatively simple analysis for noncharring ablators was developed by Matting and Chapman (ref. 140). The method of reference 140 is applicable to melting, vaporizing, or subliming surfaces, but treats only the stagnation point. Moss (ref. 11) developed a code for solving the fully viscous, ablating wall problem at and downstream of the stagnation point. Both convective and radiative heating can be treated. The coupling between the chemically reacting boundary layer and charring ablators was formulated by Kendall et al. (ref. 141). The code is known as CMA. The computation is one-dimensional; although various body shapes can be used, the upstream history of the boundary layer is ignored. The surface ablation in gases other than air can also be analyzed; for example, rocket nozzle flows, or flight through the atmospheres of other planets.

In concluding this discussion of convective heating calculation methods, it should be emphasized that theoretical methods alone are insufficient to accurately predict the high-speed heating of a vehicle's surface. Codes are not yet precise enough to be relied upon solely to compute heating in complex viscous or three-dimensional flows. However, experiments are costly, time-consuming, and frequently incapable of simulating flight conditions. The judicious use of verified codes and other theoretical procedures can greatly reduce the amount of experimental testing that is required. Only by using a combination of reliable theoretical methods supplemented by carefully conducted experiments can the heating of a vehicle be determined with a high level of confidence.

Ames Research Center
National Aeronautics and Space Administration
Moffett Field, California 94035
March 15, 1989

REFERENCES

1. Lees, L.: Laminar Heat Transfer Over Blunt-Nosed Bodies at Hypersonic Flight Speeds. Jet Propulsion, vol. 26, no. 4, Apr. 1956, pp. 259-269, 274.

2. Fay, J. A.; and Riddell, F. R.: Theory of Stagnation Point Heat Transfer in Dissociated Air. J. Aeronaut. Sci., vol. 25, no. 2, Feb. 1958, pp. 73-85, 121.

3. Beckwith, I. E.; and Cohen, N. B.: Application of Similar Solutions to Calculation of Laminar Heat Transfer on Bodies with Yaw and Large Pressure Gradient in High-Speed Flow. NASA TN D-625, 1961.

4. Cohen, N. B.: Boundary-Layer Similar Solutions and Correlation Equations for Laminar Heat-Transfer Distribution in Equilibrium Air at Velocities up to 41,100 Feet per Second. NASA TR R-118, 1961.

5. Moeckel, W. E.; and Weston, K. C.: Composition and Thermodynamic Properties of Air in Chemical Equilibrium. NACA TN-4265, 1958.

6. Hansen, C. F.: Approximations for the Thermodynamic and Transport Properties of High-Temperature Air. NACA TN-4150, 1958.

7. Dorrance, W. H.: Viscous Hypersonic Flow. McGraw-Hill Book Co., Inc., 1962.

8. Rohsenow, W. M.; Hartnett, J. P.; and Ganic, E. N., ed.: Handbook of Heat Transfer Fundamentals, Second ed., Chap. 8, Rubesin, M. W., Inouye, M. and Parikh, P. G., "Forced Convection, External Flows," McGraw-Hill Book Co., 1985.

9. Nelson, W. C., ed.: The High Temperature Aspects of Hypersonic Flow, Chap. 30, Fay, J. A., "Hypersonic Heat Transfer in the Air Laminar Boundary Layer," The Macmillan Company, 1964, pp. 583-605.

10. Rakich, J. V.; Stewart, D. A.; and Lanfranco, M. J.: Results of a Flight Experiment on the Catalytic Efficiency of the Space Shuttle Heat Shield. AIAA Paper 82-0944, June 1982.

11. Moss, J. N.:Reacting Viscous-Shock-Layer Solutions with Multicomponent Diffusion and Mass Injection. NASA TR R-411, 1974.

12. Peng, F.; and Pindroh, A. L.: An Improved Calculation of Gas Properties at High Temperatures: Air. Boeing Airplane Co. Document No. D2-11722, Dec. 1962.

13. Yos, J. M.: Transport Properties of Nitrogen, Hydrogen, Oxygen and Air to 30,000 K. AVCO Corp. Tech. Memo, RAD-TM-63-7, March 1963.

14. Horton, T. E.; and Zeh, D. W.: Effect of Uncertainties in Transport Properties on Prediction of Stagnation-Point Heat Transfer. AIAA J., vol. 5, no. 8, Aug. 1967, pp. 1497-1498.

15. Lee, J. S.; and Bobbitt, P. J.: Transport Properties at High Temperatures of CO_2-N_2-O_2-Ar Gas Mixtures for Planetary Entry Applications. NASA TN D-5476, 1969.

16. Blake, L. H.: Approximate Transport Calculations for High-Temperature Air. AIAA J., vol. 8, no. 9, Sept. 1970, pp. 1698-1701.

17. Howe, J. T.; and Sheaffer, I.: Effects of Uncertainties in the Thermal Conductivity of Air on Convective Heat Transfer for Stagnation Temperatures up to 30,000 K. NASA TN D-2678, 1965.

18. Worbs, H. E.; and Bolster, B. D.: Analytical Approximations for the Density and Viscosity of Equilibrium Air. J. Spacecraft Rockets, vol. 4, no. 6, June 1967, p. 801.

19. Gordon, S.; and McBride, B. J.,: Computer Program for Calculation of Complex Chemical Equilibrium Compositions, Rocket Performance, Incident and Reflected Shocks, and Chapman-Jouguet Detonations. NASA SP-273, 1976.

20. Hoshizaki, H.: Heat Transfer in Planetary Atmospheres at Super-satellite Speeds. ARS J., vol. 32, 1962, pp. 1544-1552.

21. Marvin, J. G.; and Deiwert, G. S.: Convective Heat Transfer in Planetary Gases. NASA TR R-224, 1965.

22. DeRienzo, P.; and Pallone, A. J.: Convective Stagnation-Point Heating for Re-Entry Speeds up to 70,000 fps Including Effects of Large Blowing Rates. AIAA J., vol. 5, no. 2, Feb. 1967, pp. 193-200.

23. Marvin, J. G.; and Pope, R. B.: Laminar Convective Heating and Ablation in the Mars Atmosphere. AIAA J., vol. 5, no. 2, Feb. 1967, pp. 240-248.

24. Chapman, G. T.: Theoretical Laminar Convective Heat Transfer and Boundary-Layer Characteristics on Cones at Speeds to 24 km/sec. NASA TN D-2463, 1964.

25. Sutton, K.; and Graves, R. A., Jr.: A General Stagnation-Point Convective-Heating Equation for Arbitrary Gas Mixtures. NASA TR R-376, 1971.

26. Compton, D. L.; and Chapman, G. T.: Two New Free-Flight Methods for Obtaining Convective-Heat-Transfer Data. NASA TM X-54014, 1964.

27. Rose, P. H.; and Stankevics, J. O.: Stagnation-Point Heat Transfer Measurements in Partially Ionized Air. AIAA J., vol. 1, no. 12, Dec. 1963, pp. 2752-2763.

28. Kemp, N. H.; Rose, P. H.; and Detra, R. W.: Laminar Heat Transfer Around Blunt Bodies in Dissociated Air. J. Aero Space Sci., vol. 26, no. 7, July 1959, pp. 421-430.

29. Vallerani, E.: Effect of Tip Blunting on Cone Laminar Heat Transfer. AIAA J., vol. 7, no. 1, Jan. 1969, pp. 145-146.

30. Rubesin, M. W.: The Effect of Boundary Layer Growth Along Swept-Wing Leading Edges. Vidya Corp., Rep. No. 4, 1958.

31. Shorenstein, M. L.; and Probstein, R. F.: The Hypersonic Leading-Edge Problem. AIAA J., vol. 6, no. 10, Oct. 1968, pp. 1898-1906.

32. Shorenstein, M. L.: Hypersonic Leading Edge Problem: Wedges and Cones. AIAA J., vol. 10, no. 9, Sept. 1972, pp. 1173-1178.

33. Boylan, D. E.: Laminar Convective Heat-Transfer Rates on a Hemisphere Cylinder in Rarefied Hypersonic Flow. AIAA J., vol. 9, no. 8, Aug. 1971, pp. 1661-1663.

34. Moss, J. N.; Cuda, V., Jr.; and Simmonds, A. L.: Nonequilibrium Effects for Hypersonic Transitional Flows. AIAA Paper 87-0404, Jan. 1987.

35. Nomura, S.: Correlation of Hypersonic Stagnation Point Heat-Transfer at Low Reynolds Numbers. AIAA J., vol. 21, no. 11, Nov. 1983, pp. 1598-1600.

36. Owen, F. K.; and Horstman, C. C.: Hypersonic Transitional Boundary Layers. AIAA J., vol. 10, no. 6, June 1972, pp. 769-775.

37. Dougherty, N. S., Jr.; and Fisher, D. F.: Boundary Layer Transition on a 10-Deg Cone: Wind Tunnel/Flight Correlation. AIAA Paper 80-0154, Jan. 1980.

38. Wilkins, M. E.; and Tauber, M. E.: Boundary-Layer Transition on Ablating Cones at Speeds up to 7 km/sec. AIAA J., vol. 4, no. 8, Aug. 1966, pp. 1344-1348.

39. Potter, J. L.: Boundary-Layer Transition on Supersonic Cones in a Aeroballistic Range. AIAA J., vol. 13, no. 3, March 1975, pp. 270-277.

40. Beckwith, I. E.: Development of a High Reynolds Number Quiet Tunnel for Transition Research. AIAA J., vol. 13, no. 3, March 1975.

41. Beckwith, I. E.; Creel, T. R., Jr.; Chen, F. J.; and Kendall, J. M.: Free-Stream Noise and Transition Measurements on a Cone in a Mach 3.5 Pilot Low-Disturbance Tunnel. NASA TP-2180, 1983.

42. Chen, F.-J.; Malik, M. R.; and Beckwith, I. E.:Comparison of Boundary Layer Transition on a Cone and Flat Plate at Mach 3.5. AIAA Paper 88-0411, Jan. 1988.

43. Softley, E. J.; Graber, B. C.; and Zempel, R. E.: Experimental Observation of Transition of the Hypersonic Boundary Layer. AIAA J., vol. 7, no. 2, Feb. 1969, pp. 257-263.

44. Whitfield, J. D.; and Iannuzzi, F. A.: Experiments on Roughness Effects on Cone Boundary-Layer Transition Up to Mach 16. AIAA J., vol. 7, no. 3, March 1969, pp. 465-470.

45. Swigart, R. J.: Roughness-Induced Boundary-Layer Transition on Blunt Bodies. AIAA J., vol. 10, no. 10, Oct. 1972, pp. 1355-1356.

46. Laderman, A. J.: Effect of Surface Roughness on Blunt Body Boundary-Layer Transition. J. Spacecraft Rockets, vol. 14, no. 4, April 1977, pp. 253-255.

47. Batt, R. G.; and Legner, H. H.: A Review of Roughness Induced Nosetip Transition. AIAA Paper-81-1223, June 1981.

48. Detra, R. W.; and Hidalgo, H.: Generalized Heat Transfer Formulas and Graphs for Nose Cone Re-Entry Into the Atmosphere. ARS J., March 1961, pp. 318-321.

49. Amirkabirian, I.; Bertin, J. J.; Cline, D. D.; and Goodrich, W. D.: Effects of Disturbances on Shuttle Transition Measurements—Wind Tunnel and Flight. AIAA Paper 85-0902, June 1985.

50. Stetson, K. F.: Effect of Bluntness and Angle of Attack on Boundary Layer Transition on Cones and Biconic Configurations. AIAA Paper 79-0269, Jan. 1979.

51. Creel, T. R., Jr.; Beckwith, I. E.; and Chen, F. J.: Transition on Swept Leading Edges at Mach 3.5. AIAA J. Aircraft, vol. 24, no. 10, Oct. 1987, pp. 710-717.

52. Hopkins, E. J.; and Inouye, M.: An Evaluation of Theories for Predicting Turbulent Skin Friction and Heat Transfer on Flat Plates at Supersonic and Hypersonic Mach Numbers. AIAA J., vol. 9, no. 6, June 1971, pp. 993-1003.

53. Cary, A. M., Jr.; and Bertram, M. H.: Engineering Prediction of Turbulent Skin Friction and Heat Transfer in High-Speed Flow. NASA TN D-7507, 1974.

54. Rubesin, M. W.; and Johnson, H. A.: A Critical Review of Skin Friction and Heat-Transfer Solutions of the Laminar Boundary Layer on a Flat Plate. Trans. ASME, vol. 71, no. 4, 1949, pp. 383-388.

55. Sommer, S. C.; and Short, B. J.: Free-Flight Measurements of Turbulent Boundary-Layer Skin Friction in the Presence of Severe Aerodynamic Heating at Mach Numbers From 2.8 to 7.0. NACA TN 3391, 1955.

56. Eckert, E. R. G.; and Drake, R. M.: Heat and Mass Transfer (2nd ed.). McGraw-Hill, 1959.

57. Van Driest, E. R.: Problem of Aerodynamic Heating. Aeronaut. Eng. Rev., vol. 15, no. 10, Oct. 1956, pp. 26-41.

58. Spalding, D. B.; and Chi, S. W.: The Drag of a Compressible Turbulent Boundary Layer on a Smooth Flat Plate With and Without Heat Transfer. J. Fluid Mech., vol. 18, pt., 1, Jan. 1964, pp. 117-143.

59. Coles, D.: The Turbulent Boundary Layer in a Compressible Fluid. Phys. Fluids, vol. 7, no. 9, Sept. 1964, pp. 1403-1423.

60. Chien, K. Y.: Hypersonic, Turbulent Skin-Friction and Heat-Transfer Measurements on a Sharp Cone. AIAA J., vol. 12, no. 11, Nov. 1974, pp. 1522-1526.

61. Cook, W. J.; and Richards, D. E.: Heat Transfer for Highly Cooled Supersonic Turbulent Boundary Layers. AIAA J., vol. 15, no. 9, Sept. 1977, pp. 1335-1337.

62. Hopkins, R. A.; and Nerem, R. M.: An Experimental Investigation of Heat Transfer from a Highly Cooled Turbulent Boundary Layer. AIAA J., vol. 6, no. 10, Oct. 1968, pp. 1912-1918.

63. Cary, A. M., Jr.: Turbulent-Boundary-Layer Heat-Transfer and Transition Measurements with Surface Cooling at Mach 6. NASA TN D-5863, 1970.

64. Neal, L., Jr.; and Bertram, M. J.: Turbulent-Skin-Friction and Heat-Transfer Charts Adapted from the Spalding and Chi Method. NASA TN D-3969, 1967.

65. Zoby, E. V.; and Graves, R. A., Jr.: Comparison of Turbulent Prediction Methods with Ground and Flight Test Heating Data. AIAA J., vol. 15, no. 7, July 1977, pp. 901-902.

66. Wilcox, D. C.; and Chambers, T. L.: Computation of Turbulent Boundary Layers on Curved Surfaces. DCW Industries Report No. DCW-R-07-01, Jan. 1976. (Also NASA CR-137853.)

67. Wilcox, D. C.: User's Guide for the EDDYBL Computer Program. DCW Industries Report No. DCW-R-14-02, Nov. 1976.

68. Wilcox, D. C.: Recent Improvements to the Spinning Body Version of the EDDYBL Computer Program. DCS Industries Report No. DCW-R-24-01, Nov. 1979. (Also NASA CR-152347.)

69. Arthur, P. D.; Shultz, H.; and Guard, F. L.: Flat Plate Turbulent Heat Transfer at Hypervelocities. J. Spacecraft Rockets, vol. 3, Oct. 1966, pp. 1549-1551.

70. Dhawan, S.; and Narasimha, R.: Some Properties of Boundary Layer Flow During the Transition from Laminar to Turbulent Motion. J. Fluid Mech., vol. 3, pt. 4, Jan. 1958, pp. 418-436.

71. Tauber, M. E.; and Adelman, H. G.: The Thermal Environment of Transatmospheric Vehicles. AIAA J. Aircraft, vol. 25, April 1988, pp. 355-363.

72. Throckmorton, D. A.: Benchmark Determination of Shuttle Orbiter Entry Aerodynamic Heat-Transfer Data. J. Spacecraft Rockets, vol. 20, May-June 1983, pp. 219-224.

73. Eaton, R. R.; and Larson, D. E.: Symmetry Plane Laminar and Turbulent Viscous Flow on Bodies at Incidence. AIAA J., vol. 13, no. 5, May 1975, pp. 559-560.

74. Rizk, Y. M.; Chaussee, D. S.; and McRae, D. S.: Computation of Hypersonic Viscous Flow Around Three-Dimensional Bodies at High Angles of Attack. AIAA Paper 81-1261, June 1981.

75. Widhopf, G. F.: Turbulent Heat-Transfer Measurements on a Blunt Cone at Angle of Attack. AIAA J., vol. 9, no. 8, Aug. 1971, pp. 1574-1580.

76. Chen, K. K.: Compressible Turbulent Boundary-Layer Heat Transfer to Rough Surfaces in Pressure Gradient. AIAA J., vol. 10, no. 5, May 1972, pp. 623-629.

77. Merzkirch, W.; Page, R. H.; and Fletcher, L. S.: A Survey of Heat Transfer in Compressible Separated and Reattached Flows. AIAA J., vol. 26, no. 2, Feb. 1988, pp. 144-150.

78. Holloway, P. F.; Sterrett, J. R.; and Creekmore, H. S.: An Investigation of Heat Transfer Within Regions of Separated Flow at a Mach Number of 6. NASA TN D-3074, 1965.

79. Keyes, J. W.; Goldberg, T. J.; and Emery, J. C.: Turbulent Heat Transfer Associated with Control Surfaces at Mach 6. AIAA J., vol. 6, no. 8, Aug. 1968, pp. 1612-1613.

80. Back, L. H.; and Cuffel, R. F.: Changes in Heat Transfer from Turbulent Boundary Layers Interacting with Shock Waves and Expansion Waves. AIAA J., vol. 8, no. 10, Oct. 1970, pp. 1871-1873.

81. Nestler, D. E.: Engineering Analysis of Reattaching Shear Layer Heat Transfer. AIAA J., vol. 11, no. 3, March 1973, pp. 390-392.

82. Alzner, E.; and Zakkay, V.: Turbulent Boundary-Layer Shock Interaction With and Without Injection. AIAA J., vol. 9, no. 9, Sept. 1971, pp. 1769-1776.

83. Matthews, R. D.; and Ginoux, J. J.: Correlation of Peak Heating in the Reattachment Region of Separated Flows. AIAA J., vol. 12, March 1974, pp. 397-399.

84. Shang, J. S.; and Hankey, W. L., Jr.: Numerical Solution for Supersonic Turbulent Flow over a Compression Ramp. AIAA J., vol. 13, no. 10, Oct. 1975, pp. 1368-1374.

85. Hung, C. M.; and MacCormack, R. W.: Numerical Solutions of Supersonic and Hypersonic Laminar Compression Corner Flows. AIAA J., vol. 14, no. 4, April 1976, pp. 475-481.

86. Lawrence, S. L.; Tannehill, J. C.; and Chaussee, D. S.: An Upwind Algorithm for the Parabolized Navier-Stokes Equations. AIAA Paper 86-1117, May 1986.

87. Tannehill, J. C.; Ievalts, J. O.; and Lawrence, S. L.: An Upwind Parabolized Navier-Stokes Code for Real Gas Flows. AIAA Paper 88-0713, Jan. 1988.

88. Back, L. H.; and Cuffel, R. F.: Shock Wave/Turbulent Boundary-Layer Interactions With and Without Surface Cooling. AIAA J., vol. 14, no. 4, April 1976, pp. 517-532.

89. Skebe, S. A.; Greber, I.; and Hingst, W. R.: Investigation of Two-Dimensional Shock-Wave/Boundary-Layer Interactions. AIAA J., vol. 25, no. 6, June 1987, pp. 777-783.

90. Hodge, B. K.: Prediction of Hypersonic Laminar Boundary-Layer/Shock-Wave Interaction. AIAA J., vol. 15, no. 7, July 1977, pp. 903-904.

91. Hung, F. T.; Greenschlag, S. N.; and Scottoline, C. A.: Shock-Wave-Boundary-Layer Interaction Effects on Aerodynamic Heating. J. Spacecraft Rockets, vol. 14, no. 1, Jan. 1977, pp. 25-31.

92. Viegas, J. R.; and Coakley, T. J.: Numerical Investigation of Turbulence Models for Shock-Separated Boundary-Layer Flows. AIAA J., vol. 16, no. 4, April 1978, pp. 293-294.

93. Nestler, D. E.; Saydah, A. R.; and Auxer, W. L.: Heat Transfer to Steps and Cavities in Hypersonic Turbulent Flow. AIAA J., vol. 7, no. 7, July 1969, pp. 1368-1370.

94. Gortyshov, Y. F.; Varfolomeev, I. M.; and Schchukin, V. K.: Study of Heat Transfer in Separated Zones Formed by Rectangular Cavities. Soviet Aeronaut., vol. 25, no. 1, 1982, pp. 33-39 (English translation by Allerton Press, New York).

95. Lamb, J. P.: Convective Heat Transfer Correlations for Planar, Supersonic, Separated Flows. Trans. ASME J. Heat Transfer, vol. 102, no. 2, May 1980, pp. 351-356.

96. Francis, W. L.: Turbulent Base Heating on a Slender Re-Entry Vehicle. J. Spacecraft Rockets, vol. 9, no. 8, Aug. 1972, pp. 620-621.

97. Bulmer, B. M.: Flight Test Correlation Technique for Turbulent Base Heat Transfer with Low Ablation. J. Spacecraft Rockets, vol. 10, no. 2, March 1973, pp. 222-224.

98. Bulmer, B. M.: Re-Entry Vehicle Base Pressure and Heat-Transfer Measurements at Mach Number at Infinity of 18. AIAA J., vol. 13, no. 4, 1975, pp. 522-524.

99. Edney, B. E.: Effects of Shock Impingement on the Heat Transfer around Blunt Bodies. AIAA J., vol. 6, no. 1, Jan. 1968, pp. 15-21.

100. Keyes, J. W.; and Morris, D. J.: Correlations of Peak Heating in Shock Interference Regions at Hypersonic Speeds. J. Spacecraft Rockets, vol. 9, no. 8, Aug. 1972, pp. 621-623.

101. Keyes, J. W.: Correlation of Turbulent Shear Layer Attachment Peak Heating Near Mach 6. AIAA J., vol. 15, no. 12, Dec. 1977, pp. 1821-1823.

102. Howe, J. T.; and Mersman, W. A.: Solutions of the Laminar Compressible Boundary-Layer Equations with Transpiration Which are Applicable to the Stagnation Regions of Axisymmetric Blunt Bodies. NASA TN D-12, 1959.

103. Low, G. M.: The Compressible Laminar Boundary Layer with Fluid Injection. NACA TN 3404, 1955.

104. Pappas, C. C.; and Okuno, A. F.: Heat-transfer Measurement for Binary Gas Laminar Boundary Layers with High Rates of Injection. NASA TN D-2473, 1964.

105. Pappas, C. C.; and Okuno, A. F.: Measurements of Skin Friction of the Compressible Turbulent Boundary Layer on a Cone with Foreign Gas Injection. J. Aero/Space Sci., May 1960, pp. 321-333.

106. Pappas, C. C.; and Okuno, A. F.: The Relation Between Skin Friction and Heat Transfer for the Compressible Turbulent Boundary Layer with Gas Injection. NASA TN D-2857, 1965.

107. Kaattari, G. E.: Effects of Mass Addition on Blunt-Body Boundary-Layer Transition and Heat Transfer. NASA TP-1139, 1978.

108. Dershin, H.; Leonard, C. A.; and Gallaher, W. H.: Direct Measurement of Skin Friction on a Porous Flat Plate with Mass Injection. AIAA J., vol. 5, no. 11, Nov. 1967, pp. 1934-1939.

109. Jeromin, L. O. F.: The Status of Research in Turbulent Boundary Layers with Fluid Injection. Progr. Aeronaut. Sci., vol. 10, 1970, pp. 65-189.

110. Putz, K. E.; and Bartlett, E. P.: Heat-Transfer and Ablation-Rate Correlations for Re-Entry Heat-Shield and Nosetip Applications. J. Spacecraft Rockets, vol. 10, no. 1, Jan. 1973, pp. 15-22.

111. Chin, J. H.: Shape Change and Conduction for Nosetips at Angle of Attack. AIAA J., vol. 13, no. 5, May 1975, pp. 599-604.

112. Grabow, R. M.; and White, C. O.: Surface Roughness Effects on Nosetip Ablation Characteristics. AIAA J., vol. 13, no. 5, May 1975, pp. 605-609.

113. Kobayashi, W. S.; and Saperstein, J. L.: Low Temperature Ablator Tests for Shape Stable Nosetip Applications on Maneuvering Reentry Vehicles. AIAA Paper 81-1061, June 1981.

114. Gold, H.; DiCristina, V.; and Pallone, A. J.: Nosetip Cooling by Discrete Fluid Injection. AIAA Paper 68-1141, Dec. 1968.

115. Libby, P. A.; and Kassoy, D. R.: Laminar Boundary Layer at an Infinite Swept Stagnation Line with Large Rates of Injection. AIAA J., vol. 8, no. 10, Oct. 1970, pp. 1846-1851.

116. Wortman, A.; and Mills, A. F.: Mass Transfer Effectiveness at Three-Dimensional Stagnation Points. AIAA J., vol. 9, no. 6, June 1971, pp. 1210-1212.

117. Wortman, A.: Foreign Gas Injection into Three-Dimensional Stagnation Point Flows. J. Spacecraft Rockets, vol. 9, no. 6, June 1972, pp. 428-434.

118. Wortman, A.: Heat and Mass Transfer on Cones at Angles of Attack. AIAA J., vol. 10, no. 6, June 1972.

119. Inger, G. R.; and Gaitatzes, G. A.: Strong Blowing into Supersonic Laminar Flows Around Two-Dimensional and Axisymmetric Bodies. AIAA J., vol. 9, no. 3, March 1971, pp. 436-443.

120. Demetriades, A.; Laderman, A. J.; Von Seggern, L.; Hopkins, A. T.; and Donaldson, J. C.: Effect of Mass Addition on the Boundary Layer of a Hemisphere at Mach 6. J. Spacecraft Rockets, vol. 13, no. 8, Aug. 1976, pp. 508-509.

121. Wimberly, C. R.; McGinnis, F. K. III; and Bertin, J. J.: Transpiration and Film Cooling Effects for a Slender Cone in Hypersonic Flow. AIAA J., vol. 8, no. 6, June 1970, pp. 1032-1038.

122. Park, C.: Injection Induced Turbulence in Stagnation-Point Boundary Layers. AIAA J., vol. 22, no. 2, Feb. 1984, pp. 219-225.

123. Lundell, J. H.; and Dickey, R. R.: Ablation of ATJ Graphite at High Temperatures. AIAA J., vol. 11, no. 2, Feb. 1973, pp. 216-222.

124. Lundell, J. H.; and Dickey, R. R.: Ablation of Graphitic Materials in the Sublimation Regime. AIAA J., vol. 13, no. 8, Aug. 1975, pp. 1079-1085.

125. Ziering, M. B.: Thermochemical Ablation of Ceramic Heat Shields. AIAA J., vol. 13, no. 5, May 1975, pp. 610-616.

126. Rohsenow, W. M.; Hartnett, J. P.; and Ganic, E. N., eds.: Handbook of Heat Transfer Applications, Chap. 1, Hartnett, J. P., "Mass Transfer Cooling." Second ed., McGraw-Hill Book Co., 1985.

127. Thompson, R. A.; Zoby, E. V.; Wurster, K. E.; and Gnoffo, P. A.: An Aerothermodynamic Study of Slender Conical Vehicles. AIAA Paper 87-1475, June 1987.

128. Chaussee, D. S.: NASA Ames Research Center's Parabolized Navier-Stokes Code: A Critical Evaluation of Heat-Transfer Predictions. AIAA Paper 87-1474, June 1987.

129. Chaussee, D. S.; and Rizk, Y. M.: Computation of Viscous Hypersonic Flow Over Control Surfaces. AIAA Paper 82-0291, Jan. 1982.

130. Rizk, Y. M.; Chaussee, D. S.; and McRae, D. S.: Computation of Hypersonic Viscous Flow Around Three-Dimensional Bodies at High Angles of Attack. AIAA Paper 81-1261, June 1981.

131. Balakrishnan, A.; and Chaussee, D. S.: A Computational Study of Heat Transfer for Laminar Hypervelocity Flows. AIAA Paper 88-2666, June 1988.

132. Prabhu, D. K.: A New Parabolized Navier-Stokes Code for Chemically Reacting Flow Fields. Ph.D. Dissertation, Iowa State Univ., Ames, IA, 1987.

133. Prabhu, D. K.; Tannehill, J. C.; and Marvin, J. G.: A New PNS Code for Chemical Nonequilibrium Flows. AIAA Paper 87-0284, Jan. 1987.

134. Prabhu, D. K.; Tannehill, J. C.; and Marvin, J. G.: A New PNS Code for Three-Dimensional Chemically Reacting Flows. AIAA Paper 87-1472, June 1987.

135. Tannehill, J. C.; Ievalts, J. O.; Prabhu, D. K.; and Lawrence, S. L.: An Upwind Parabolized Navier-Stokes Code for Chemically Reacting Flows. AIAA Paper 88-2615, June 1988.

136. Palmer, G.: An Implicit Flux-Split Algorithm to Calculate Hypersonic Flowfields in Chemical Equilibrium. AIAA Paper 87-1580, June 1987.

137. Palmer, G.: An Improved Flux-Split Algorithm Applied to Hypersonic Flows in Chemical Equilibrium. AIAA Paper 88-2693, June 1988.

138. Edwards, T.; Chaussee, D.; Lawrence, S.; and Rizk, Y.: Comparisons of Four CFD Codes as Applied to a Hypersonic All-Body Vehicle. AIAA Paper 87-2642, Aug. 1987.

139. Murray, A. L.: Facilitation of the BLIMP Computer Code and User's Guide. Prep. by Acurex Corp., Aerotherm Div., Huntsville, AL, for Flight Dynamics Laboratory, USAF Systems Command, Wright-Patterson AFB, OH, AFWAL-TR-86-3101, vols. 1 and 2, Jan. 1987.

140. Matting, F. W.; and Chapman, D. R.: Analysis of Surface Ablation of Noncharring Materials with Description of Associated Computing Program. NASA TN D-3758, 1966.

141. Kendall, R. M.; Bartlett, E. P.; Rindal, R. A.; and Moyer, C. B.: An Analysis of the Coupled Chemically Reacting Boundary Layer and Charring Ablator (Parts I-VI). NASA CR-1060-1065, 1968.

APPENDIX

Listed below are some useful conversion factors.

1 Btu	=	1054.8 J
1 Btu/lb	=	2325.4 J/kg
1 ft	=	0.3048 m
1 lb	=	0.4536 kg
1 slug/ft^3	=	515.2 kg/m^3
1 W	=	9.4805(10^{-4}) Btu/sec
1 W/cm^2	=	0.88076 Btu/ft^2 sec
1 W/m^2	=	8807.6 Btu/ft^2 sec

NASA National Aeronautics and Space Administration

Report Documentation Page

1. Report No.	2. Government Accession No.	3. Recipient's Catalog No.
NASA TP-2914		

4. Title and Subtitle	5. Report Date
A Review of High-Speed, Convective, Heat-Transfer Computation Methods	July 1989
	6. Performing Organization Code
7. Author(s)	8. Performing Organization Report No.
Michael E. Tauber	A-89042
	10. Work Unit No.
	506-40-11
9. Performing Organization Name and Address	11. Contract or Grant No.
Ames Research Center Moffett Field, CA 94035	
	13. Type of Report and Period Covered
12. Sponsoring Agency Name and Address	Technical Paper
National Aeronautics and Space Administration Washington, DC 20546-0001	14. Sponsoring Agency Code

15. Supplementary Notes

Point of Contact: Michael E. Tauber, Ames Research Center, MS 230-2, Moffett Field, CA 94035
(415) 694-6086 or FTS 464-4126

16. Abstract

The objective of this report is to provide useful engineering formulations and to instill a modest degree of physical understanding of the phenomena governing convective aerodynamic heating at high flight speeds. Some physical insight is not only essential to the application of the information presented here, but also to the effective use of computer codes which may be available to the reader. The paper begins with a discussion of cold-wall, laminar boundary layer heating. A brief presentation of the complex boundary layer transition phenomenon follows. Next, cold-wall turbulent boundary layer heating is discussed. This topic is followed by a brief coverage of separated flow-region and shock-interaction heating. A review of heat protection methods follows, including the influence of mass addition on laminar and turbulent boundary layers. The paper concludes with a discussion of finite-difference computer codes and a comparison of some results from these codes. An extensive list of references is also provided from sources such as the various AIAA journals and NASA reports which are available in the open literature.

17. Key Words (Suggested by Author(s))	18. Distribution Statement
Aerodynamic heating High-speed aerodynamic heating Heat-transfer computations	Unclassified – Unlimited Subject category: 34

19. Security Classif. (of this report)	20. Security Classif. (of this page)	21. No. of pages	22. Price
Unclassified	Unclassified	36	A03

For sale by the National Technical Information Service, Springfield, Virginia 22161